Influence of Cerium Doping on the Physical Characteristics of WO_3 Nanomaterials

By

Muhammad Saleem

Supervised

By

Dr. Javed Iqbal Saggu

DEPARTMENT OF PHYSICS

QUAID-I-AZAM UNIVERSITY

ISLAMABAD, PAKISTAN

2017

This work is submitted as a dissertation in partial fulfilment of the requirement for the degree of

MASTER OF PHILOSOPHY

IN

PHYSICS

To The

DEPARTMENT OF PHYSICS

QUAID-I-AZAM UNIVERSITY

ISLAMABAD, PAKISTAN

2017

CERTIFICATE

This is to certify that the experimental work in this dissertation bearing the title "***Influence of Cerium Doping on the Physical Characteristics of WO_3 Nanomaterials***" has been carried out by ***Mr. Muhammad Saleem*** under my supervision in Laboratory of Nanoscience and Technology (LNT), Department of Physics, Quaid-i-Azam University, Islamabad, Pakistan.

Supervisor:

Dr. Javed Iqbal Saggu
Associate Professor
Department of Physics
Quaid -i- Azam University
Islamabad, Pakistan.

Submitted Through:

Prof. Dr. Arif Muntaz
Chairman
Department of physics
Quaid -i- Azam University
Islamabad, Pakistan.

I Dedicate This Work

To

My Beloved Parents and Elder Brother

Hamayun Khan

Acknowledgment

In the name of Allah, the Beneficent, the Merciful. All praises is due to Allah; we praise him, seek His help, and ask for His forgiveness. I am very thankful to my Allah who gives me strength, courage and guidance to complete this research and the most respectable and ideal for every Muslim Prophet Muhammad (Peace Be Upon Him).

It times to show my inner most feeling for my respectable supervisor **Dr. Javed Iqbal Saggu**. He deserves praise for his guidance to me, not only in research but also in moral and social life. I am grateful to him for listening to my ideas with interest and patience and guiding me with his precious knowledge. He always encourages and shows me my inner potential. I feel it's my goodness to work under the supervision of him. Indeed he is a remarkable supervisor.

In journey of my research I am very thankful to my research fellow Sohail for his sincere support and help during my research. It is impossible for me, to forget the kindness and sincerity of Jahangir Ali (*Chemistry department*). I am also extending my thanks to our seniors Dr. Fazal Abbas, Faisal Mehmood, Waheed Ahmed, Kashif and mam Sobia Jabeen for their kind attitude and guidance. In last but not least i say special thanks to our juniors, Abdul Qadir and Ghulam Muhauddin Sabir who give me respect and help me when i need it.

Thanks to my all family members especially to my mother and father who always with me in every loose and tight moments of my life. Once again I am thankful to my parents, teaching me values of life and make possible for me to achieve this dream of my life. I am very thankful to my dear sisters for supporting me in all respect and providing me environment to do my research. I would like to remember my younger brother Muhammad Usman to give me good time throughout my research. I am very thankful to my elder brother **Hamayun Khan** who supports me beyond my expectations in all respect and teach me a lot of things form his life.

Muhammad Saleem

Abstract

In this work, $Ce_xW_{1-x}O_3$ nanoparticles have been synthesised using simple and cost effective co-precipitation method. The concentration of Cerium dopant in Tungsten Oxide host matrix have been varied as 0%, 1%, 3%, 5%, 8% and 10% at the time of preparation. In order to get good crystallites and fine structure, the prepared samples have been annealed at optimized temperature 600^oC. The crystal structure, morphology, optical band gap, surface chemistry and vibrational modes characteristics at room temperature have been studied via XRD, SEM, UV-Vis, FTIR and Raman spectroscopy techniques respectively. The structural investigations have clearly revealed that the synthesized samples are in ordering of monoclinic structuring and Cerium is successfully doped into host matrix without forming any tiny cluster. The morphological examinations have depicted that the prepared samples are comprised of spherical nanoparticles with average particle size of 80 nm. FTIR technique has identified the presence of O-H and O-W-O type bonding. The vibrational study through Raman further confirms the absence of impurities and observed to be consistent with the results of XRD and FTIR investigations. The shift and suppression in vibrational modes of host material as function of Cerium doping may be due to the presence of defects. It is interestingly found that the band gap is significantly tailored with Cerium doping which may be assigned to defects and size of nanoparticles. Methylene blue (MB) is a toxic textile industrial wastewater material and it is very harmful for aquatic lives. The prepared Tungsten Oxide and Cerium doped Tungsten Oxide nanoparticles have shown excellent sun light driven photocatalytic activities against MB. The prepared Cerium doped Tungsten Oxide nanoparticles as a sun light driven photocatalyst, can be used for worldwide purification of wastewater.

Table of Contents

List of Figures

List of Tables

Chapter No. 1

INTRODUCTION

Nanoscience and nanotechnology are names for understanding and controlled manipulation of structures and phenomena that have nanoscale dimensions. The word "**Nano**" which is prefix, means one billionth of a unit of measure. Nanoscience and technology enable to make and explore design-based artificial structures that do not exist in nature such as metamaterial and metasurface. Nanotechnology has deep impact over scientific and technological fields from natural science to life sciences.

1.1 Brief history of Nanoscience and Nanotechnology

The people in ancient time were familiar with some effects of non-intentionally made nanoscale materials. The **stained glass windows** and **piece of Roman glasswork** are examples of a manmade nano processes in ancient time shown in fig 1.1. That time no one familiar with the knowledge of nanoscience, they did not know how and why the properties of gold change in stained glass!

Figure 1.1: a) Stained glass b) Lycurgus cup [1].

For the first time in 1959 Feynman gives the concept of nanotechnology during his lecture as;

"***There is plenty of room at the bottom***"

Feynman mentioned the idea for generation of nanoscale devices to manipulate, control, and image matter at nanoscale. After Feynman in 1974 Norio Taniguchi used the term nanotechnology and predicted its use in integrated circuits (ICs), mechanical devices and memory chips. Nanotechnology emerged in 1980s with the invention of Scanning Tunnelling Microscopy (SEM). In 1986, E. Drexler give up thrust to nanotechnology with publishing his book "**Vehicles of creation: The arrival of the Nanotechnology era**".

1.2 Nanoscience and Nanotechnology

The study of properties of objects that having size at nanoscale, lies in nanoscience while the efficient utilization of these properties is called nanotechnology. Nanoscience and nanotechnology get high importance in different fields of science. Nanoscience is an "interdisciplinary science" which means that it involves concepts of more than one discipline such as Chemistry, Biology, Biochemistry and Physics etc. Nanoscience is a "horizontal-integrating interdisciplinary science that cuts across all vertical sciences and engineering disciplines as depict in fig 1.2.

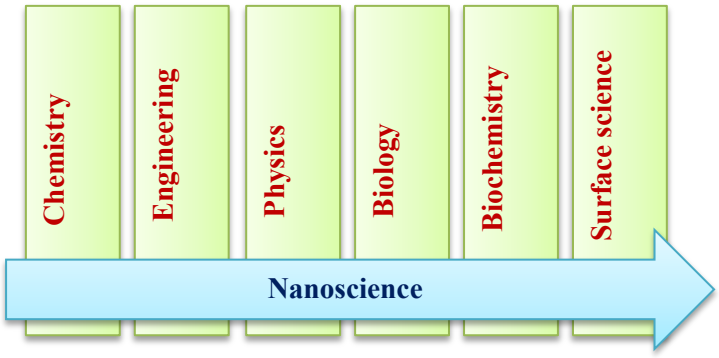

Figure 1.2: Nanoscience cuts all vertical science and engineering disciplines.

The nanoscience provides explanation for changing the properties at nanoscale. Nanoscience is mostly associated with quantum, electron and photon behaviour at nanoscale. The researchers are interesting in nanostructures due to many reasons, the first is usually small structure properties mystify us. Like how the flagellar motor works? How electrons move in organometallic nanowires? Second the preparation of nanostructures is thrilling compare to structures at large scale etc. It provides the basis for nano electronic and photonic devices [2].

Nanotechnology is the application of nanoscience especially in industrial and commercial objectives. All industrial sectors rely on materials and devices made of atoms and molecules. In principle, all materials can be improved with nanomaterials and all industries can be benefit from nanotechnology.

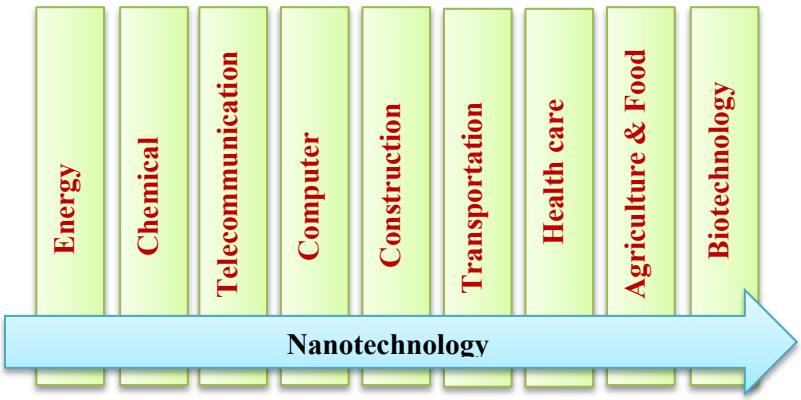

Figure 1.3: Nanotechnology is horizontal-enabling convergent technology cross all vertical industrial sectors.

Nanotechnology is horizontal-enabling convergent technology. They are "horizontal" because in fig 1.3, they cut across numerous industrial sectors. They are "enabling" since they provide the platform, the tools to realise certain products and are "convergent" because they bring together sectors of science that were previously separated.

The field of nanoscience and nanotechnology upgrades progressively. Nanotechnology allows us to design cheap and good quality products. In future computer controlled nano machines are predicted. The size of these machines will be much smaller than a dust particle. Surgeons will be able to perform surgery at the cellular and molecular level using nano machines. Furthermore, nanomaterials have good response for different gases, and used as a gas sensor [3]. The quality of environment improves using nanomaterial, the pollutants can be detect, prevent and remove from environment. With the help of material science, the toxicity of industrial wastes (such as herbicides, pesticides, detergents and organic dyes) can be killed and make them nontoxic [4-7]. The nanotechnology is also efficiently used in ware fare, formation of smart weapons and bullet proof jacket etc.

1.3 Types of materials

On the bases of energy band theory, the materials can be divided into following categories;

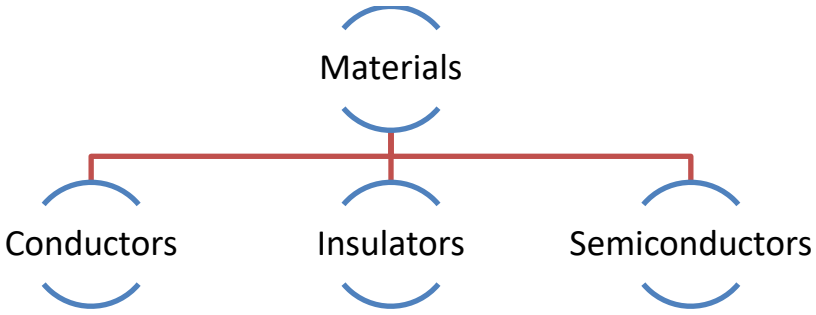

Figure 1.4: Materials classification.

1.3.1 Conductors

These are those materials, through which electricity easily pass and offers very low resistivity of the order of 10^{-8} Ω.m at room temperature. However, from energy band structure conductors are those material having overlapped conduction and valence band

as depicted in fig 1.5. Hence there is no band gap between conduction band (C.B) and valence band (V.B), for these materials. At high temperature, the resistivity of conductors increases due to increase in number of collision between electron-electron and electron-atom. That is why conductors having positive temperature coefficient. The typical examples of conductor are Fe, Al, Au, Ag and Cu etc.

1.3.2 Insulators

Materials, they don't allow electricity to pass through it are known as insulators. Such materials have very large resistivity of the order of 10^{16} Ω.m. According to band structure, insulators have very wide band gap (>3eV) between V.B and C.B. In such large band gap material, electrons have insufficient energy to populate the conduction band. The glass, rubber and ceramics are common examples of insulator.

1.3.3 Semiconductors

Semiconductors are those materials which have intermediate electrical conductivity compare to conductors and insulators. The typical resistivity of semiconductors is of the order of 10^{-3} Ω.m. Form band theory, there is medium (≤3eV) band gap between V.B and C.B for semiconductor materials. When semiconductors are exposed to high temperature their conductivity increases, because electron from the valence band can easily excited to conduction band by the provision of thermal energy. The temperature coefficient for semiconductors is positive. Si and Ge are the typical examples of semiconductors.

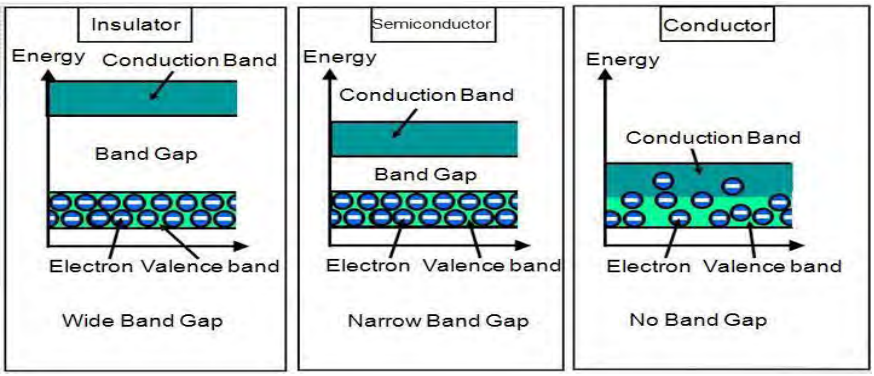

Figure 1.5: Band structure of conductor, semiconductor and insulator [8].

1.4 Types of Semiconductors

On the basis of band gap structure, the semiconductors are of two types depending on the relative maxima of V.B and the relative minima of C.B.

1.4.1 Direct Band Gap Semiconductors

A semiconductor for which maxima of V.B and minima of C.B lies on the same vertical line or both have the same "k" value is called direct band gap semiconductor. When a photon with sufficient energy falls on direct band gap semiconductor it produces electron-hole pair, and the mechanism is shown in fig 1.6. The incoming photons only taking part in electron excitation processes, they don't yield heating effects. That is why in optoelectronic devices (like in LEDs) production, the preference is given to direct band gap semiconductors. The relation of absorption coefficient to photon energy and band gap for direct band gap semiconductor is given in equation 1.1.

$$\alpha \sim (h\upsilon - E_g)^{1/2} \qquad (1.1)$$

Where "α" is absorption coefficient "hυ" is the incoming photon energy "E_g" is band gap energy.

The examples of direct band gap semiconductors are Gallium-Arsenide (GaAs), Zinc Oxide (ZnO) and Indium-Arsenide (InAs).

1.4.2 Indirect Band Gap Semiconductors

If the relative maxima of V.B and relative minima of C.B don't lies on a same vertical line or having different "k" value, called indirect band gap semiconductors. In such semiconductors, when a photon of sufficient energy couples with phonon it creates electron-hole pair as depicted in fig 1.6. The incident photon loses some of its energy in form of heat in indirect band gap semiconductors and due to this heat factor, it less usually used for optoelectronic devices. The relation of absorption coefficient for indirect band gap semiconductor is given in equation 1.2.

$$\alpha \sim (h\upsilon - E_g \pm E_{phonon})^2 \qquad (1.2)$$

In equation 1.2, "E_{phonon}" is phonon energy. The plus minus ($\pm$) sign indicates the emission or absorption of phonon energy. Examples of indirect band gap semiconductors are Silicon (Si) Tungsten Oxide (WO_3) and Germanium (Ge).

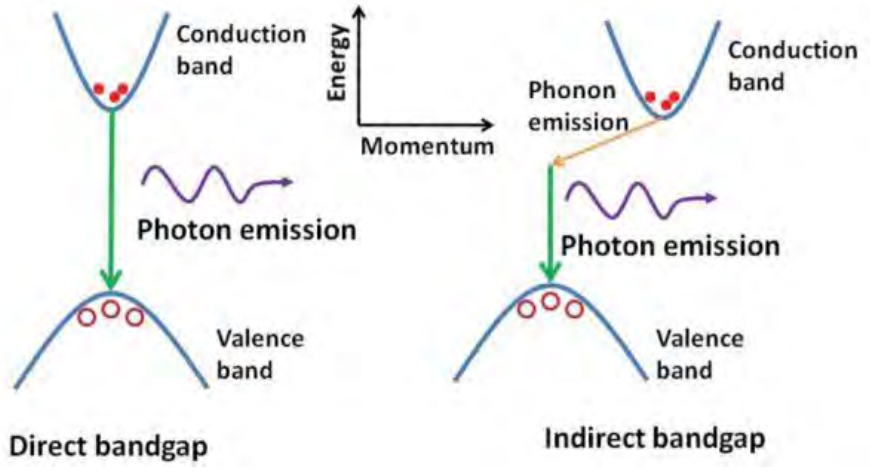

Figure 1.6: Recombination in direct and indirect bandgap semiconductors [9].

1.5 Impurity effects on energy band gap

Impurities in semiconductor material affect the electronic band transitions. The semiconductor materials having impurity exhibits multiple peaks in their absorption spectra. These peaks are due to the extra energy levels induced by impurity states between valence and conduction band. These extra energy levels are either just above the valence band or just below the conduction band, depending on the type of impurity. A donor type impurity (P, As, Sb) creates an energy level just below the conduction band while an acceptor type impurity (Al, Ga, In) generates an energy level just above the valence band. The levels generated by donor and acceptor type impurities lead to additional transition other than $E_C \rightarrow E_V$, depicted in fig 1.7.

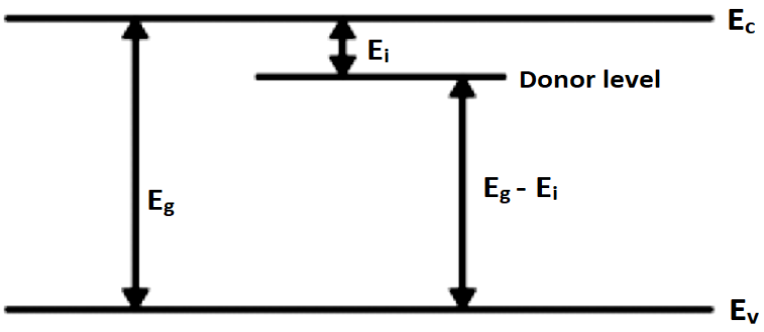

Figure 1.7: band gap structure with donor level [8].

The donor electrons from energy level E_i excites to conduction band E_c with incoming photons of energy $h\upsilon \approx E_c - E_i$, and the electrons that lie in valence band can also be excited to donor band via photons having energy $h\upsilon \approx (E_c - E_i) - E_c$. If the concentration of impurity in semiconductor is larger enough, an impurity level in absorption spectra will be observed.

1.6 Quantum Confinement (QC)

In bulk materials, the electrons can move through the bulk of material. But as the size of material decreases the electron gets more and more confined to move in limited

space. This act with electron is known as Quantum confinement effect. In QC the band structure is affected via particle size. The QC effect strongly occurs when size of crystal is smaller than Bohr radius (3nm for WO_3). [10]. According to free electron model electronic states vary as,

$$E_g \propto \frac{1}{L^2} \quad (1.3)$$

Where "E_g" is the band gap energy, "L" is length of box. It is clear from equation 1.3 that by decreasing the size of particle band gap increases as depicted in fig 1.8 [11].

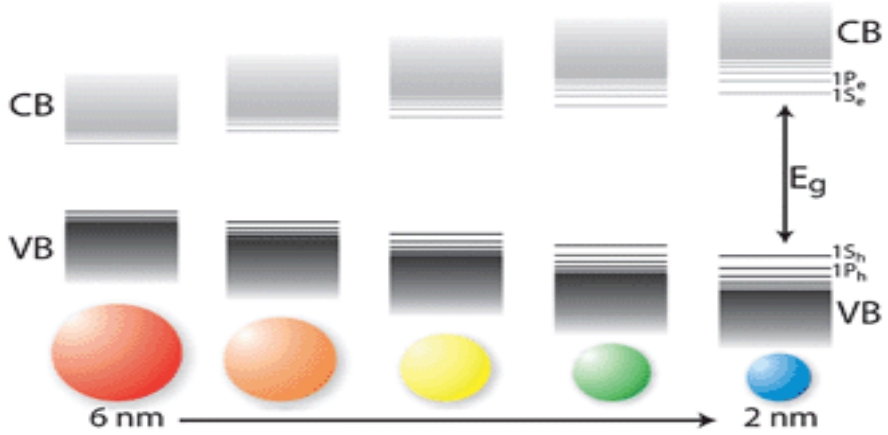

Figure 1.8: Dependence of band gap on particle size [12].

1.7 Surface to volume ratio

Surface to volume ratio is another important parameter regarding change in properties of material at nanoscale. The decrease in size of material increases the surface area. As reduce size, all most all atoms emerge on the surface. To show more explicitly the phenomena, we take the example of sphere and find its surface to volume ratio by reducing radius.

Let consider a sphere of radius "R" having volume "V" and surface area "S" as shown in fig 1.9.

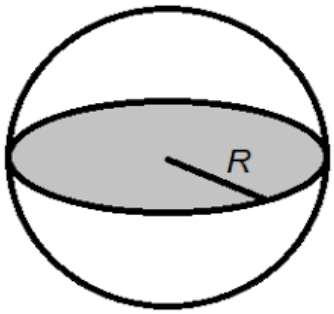

Figure 1.9: Sphere of radius "R".

$$\text{Area of the sphere} = 4\pi R^2 \quad (1.3)$$

$$\text{Volume of the sphere} = \frac{4}{3}\pi R^3 \quad (1.4)$$

Dividing equation (1.3) on equation (1.4)

$$\frac{Surface\ area}{Volume} = \frac{4\pi R^2}{(4/3\pi R3)} = \frac{3}{R}$$

Or

$$\frac{\text{Surface area}}{\text{Volume}} \propto \frac{1}{R} \quad (1.5)$$

It is clear from equation 1.5, that ratio of surface to volume depends only on radius "R". Furthermore equation 1.5 shows that there is invers relation between surface to volume ratio and radius "R". That is why one can increase the surface area by decreasing the volume of sphere.

1.8 Nanomaterials

The material with one, two or three external in the nano domain dimensions are known as nanomaterial. In making nanomaterials, the physiochemical characteristics of materials change significantly. The resulting material shows promising technological

applications. When the size of material decreases to nanometer, there is an increase in surface area in relation to the volume. Therefore, most of the atoms and molecules sit down on the surface and yields high surface reactivity. The mobility of electrons, electrons-holes and excitons significantly influence the nanomaterials due to small size effect.

1.9 Classification of Nanomaterials

Due to large verity of nanomaterials it requires to classify in different groups. Nanomaterials can be classified on the bases of dimensionality as,

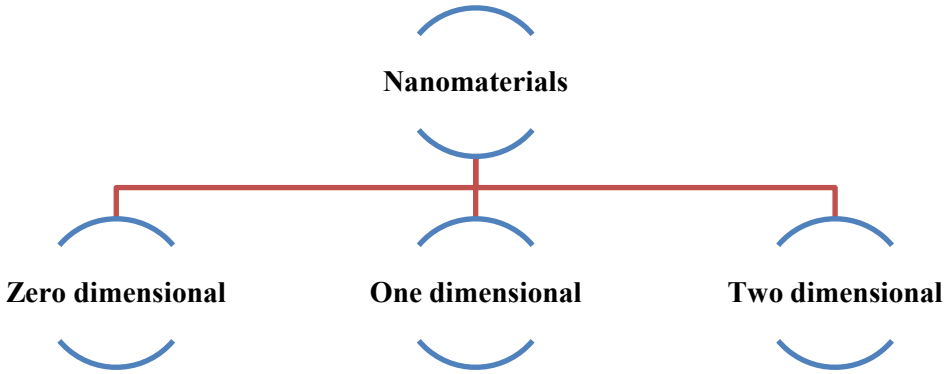

Figure 1.10: Classification of nanomaterials.

1.9.1 Zero Dimensional (0D) Nanomaterials

0D nanomaterials have all dimensions in nanometres and there is no dimension which is out of nanoscale. A verity of chemical and physical techniques has been introduced for synthesis of 0D nanomaterials, to have controlled morphology and dimensionality. Example of 0D nanomaterials is quantum dots and its typical image given in fig 1.11. These quantum dots are applicable in field of light emitting diode, single electron transistor, laser and solar cells [12-18].

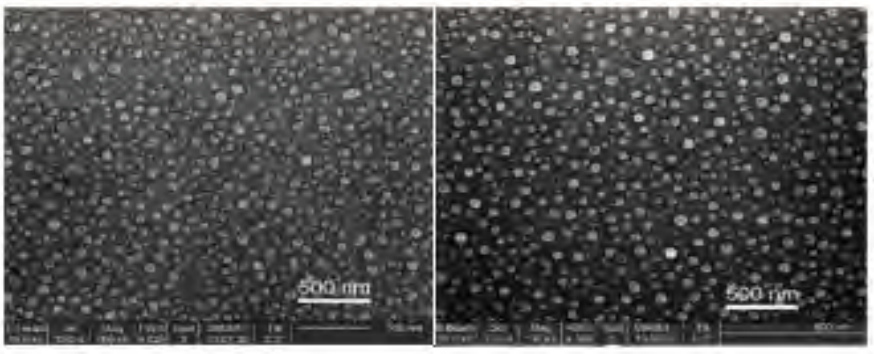

Figure 1.11: 0D images (Quantum dots) [13].

1.9.2 One Dimensional (1D) Nanomaterials

In 1D nanomaterial, two sides are at nanoscale and one is except than nanometer as shown in fig 1.12. 1D nanomaterial has potential to show important role in fabricating the electronic, optoelectronic and EEDs devices at nanoscale dimension. The examples of 1D nanomaterials are nanowires, nanotubes, nanorods, nanobelts, nanoribbons and hierarchical nanostructures [19].

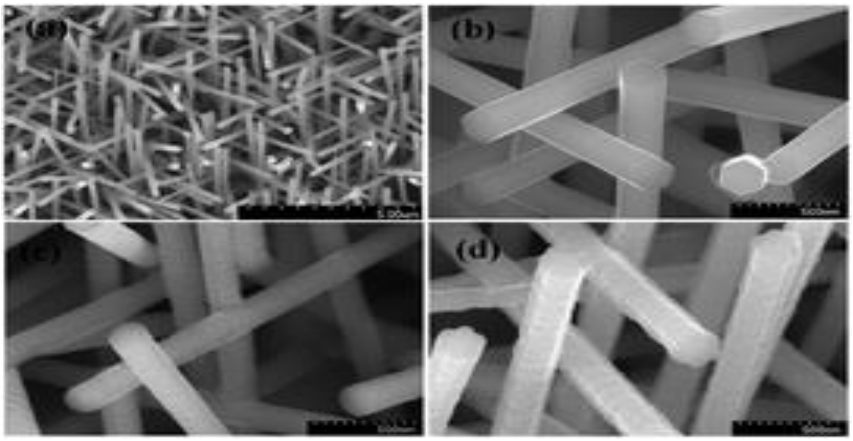

Figure 1.12: 1D images of ZnO [14].

1.9.3 Two Dimensional (2D) Nanomaterials

These are the nanostructures which have one dimension in nanometre and two larger than nanometre [14]. 2D nanomaterial possesses very unique shapes dependent properties. These novel properties can be utilized for building blocks of nano devices [20-

22]. The applications of 2D nanomaterials are photocatalysts, sensors, nanocontainers, nanoreactor, and templates for 2D designs [23]. Its examples are nanosheets, nanowalls and nanoplats. Nanoplates are shown in fig 1.13.

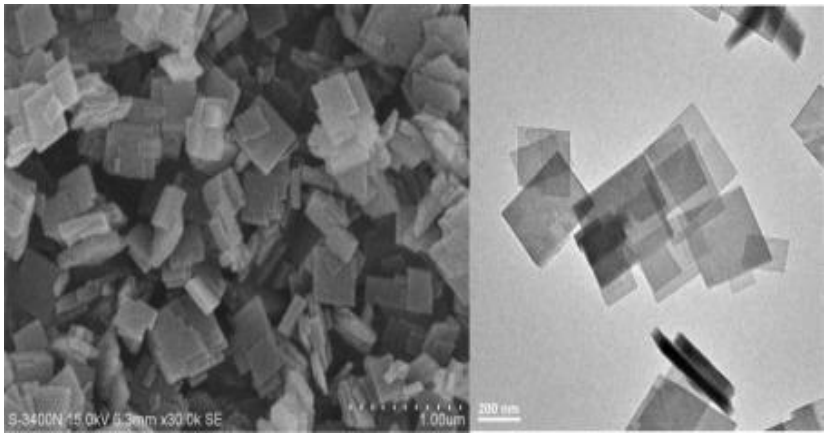

Figure 1.13: 2D nanostructures [19].

1.10 Nanomaterial Properties

Some of the basic physical properties of nanomaterials are briefly discussed here one by one.

1.10.1 Chemical properties

The chemical properties of nanomaterials depend on many parameters like chemical composition, surface area, morphology, energy band and activation energy etc. Most of chemical reactions take place on the surface of nanomaterials such as photocatalytic degradation processes. Photocatalytic degradation activity of nanomaterials increases by increasing their surface area. Sungpanich at al [24] synthesised WO_3 nanomaterials with different surface area, and reported that WO_3 nanomaterials possess large surface area have good photocatalytic degradation ability. It is also reported that this activity of nanomaterials can be further enhanced by doping suitable dopant with optimized quantity in host matrix. It is noted that zinc (Zn), platinum (Pt), silver (Ag) and Cerium(Ce) metals doping in WO_3 nanomaterial improves the

photocatalytic activity due to increase in its surface area for more chemical reactions because doping [25, 26].

1.10.2 Optical properties

Optical properties of material give information how they behave with light. Many optical properties are often closely related with electric and electronic properties of material. The optical properties of the nanomaterials are greatly dependent upon their size, shape and morphology. When light impinges on nanomaterial it generates electron-hole pair and reemits light as result of electron-hole pair recombines. As we know that the band gap of nanomaterials increase due to QC effect. One can expect that the wavelength of emitted photon from nanoparticles will be shorter than bulk which is known as blue shift in literature. In band gap engineering, the emission spectrum of quantum well is tuned by changing the dimension of quantum well. Different quantum well structures are used to improve the performance of LEDs.

1.10.3 Electrical properties

The electrical properties of nanomaterial can be explained in terms of its parameters like, density of states, band gap, conductivity and dielectric constant.

1.10.3.1 Density of states

The electrical properties of a material strongly depend on density of states (DOS) of that material. It is a very useful concept using frequently in condense matter Physics to derive a number of physical properties like specific heat, photon emission and absorption, magnetic susceptibility, concentration of electrons and holes in semiconductor and thermal and electrical conductivities. DOS gives the number of electronic states at certain energy level ready for occupying electrons. DOS usually has

maximum value at the mid of band and drop to zero at the band boundaries. At nanoscale, the DOS function "D(E)" is very sensitive to spatial dimensions of the material. The relation between "D(E)" and energy "E" for different spatial dimensions are given in Table 1.1.

Table1.1: Relation between "D(E)" and "E" for different dimensions.

Dimension	D(E)
0D (Quantum dots)	$\propto \delta(E)$
1D (Quantum wire)	$\propto E^{-1/2}$
2D Quantum well)	step function
3D (bulk)	$\propto E^{1/2}$

The plots of DOS function for 0D, 1D, 2D and 3D material are shown in fig 1.14.

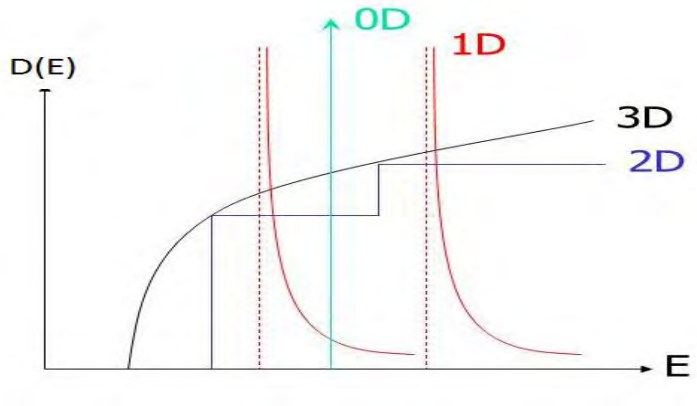

Figure 1.14: Distribution of energy states in 0D, 1D, 2D and 3D materials [27].

The number of particles "n" in a particular energy level of nanomaterial, specific heat capacity "C" and thermal conductivity "k" for nanomaterial can be determined using equations;

$$\boldsymbol{n = \int f(E)D(E)\,dE} \qquad \textbf{(1.6)}$$

$$C = \frac{\partial}{\partial T} \int Ef(E)D(E)dE \quad (1.7)$$

$$k = \frac{\partial}{\partial T} \int Ef(E)D(E)v(E)\Lambda(E)dE \quad (1.8)$$

Where "f(E)" is distribution function, "d" is the dimensionality, "v" is sound velocity and "Λ" is mean free path. From equations 1.6 to 1.8, it is clear that at nanoscale properties like "n", "C" and "k", directly depends on DOS

1.10.3.2 Band gap

The energy separation between conduction and valence bands is known as band gap. In matter, electron can't stay in gap between conduction and valence bands therefore it also called as forbidden gap or region. Band gap of nanomaterials can be quite different than bulk materials and new features in band gap can be observed at nanoscale. The band gap increases in nanomaterial due to QC effect as discussed in earlier section. Moreover the continuous band splits into discrete levels due to size effect in nanomaterials.

1.10.3.3 Conductivity

It is the ability of material that how easily electricity can pass through these materials. Usually the conductivity increase with decreasing size it has been observed that the conductivity of gold nanoparticles (GNPs) increases by decreasing the size, and decrease as particle size increase due to localized charge distribution in medium. [28]

1.10.3.4 Dielectric constant

The dielectric constant of a material is the measure of its response to external electric field. It has been observed that along with other physical properties, the dielectric response of material is also greatly affected by reducing its size down to nanoscale. Guo

et al [28] found that the dielectric response increases by decreasing the size of GNPs and vice versa. This can be attributed to the orientation of dipoles in GNPs in the direction of applied field.

1.11 Metal Oxide Nanomaterials

On earth, metals exist in their different compounds like chlorides, nitrides and oxides naturally. When metal combines with oxygen it forms their oxides. Oxygen has higher electronegativity and it takes electrons from metals which have high electron affinity. Examples of metal oxides nanomaterials are Titanium Oxide (TiO_2), Zinc Oxides (ZnO), Copper Oxides (CuO), Magnesium Oxides (MnO), Aluminium Oxides (Al_2O_3), Iron Oxides (Fe_2O_3, Fe_3O_4) ,Indium Oxides (In_2O_3) and Tungsten Oxide (WO_3). Metal oxides are used in about one third of consumer products like paints (TiO_2), cosmetics (TiO_2, ZnO), industrial operation (Al_2O_3, MnO_2) and medical (Al_2O_3, Fe_2O_3, Fe_3O_4) [29-34]. Metal oxide nanomaterials are mostly act as a photocatalyst. The advantages of using nanomaterials as photocatalytic system are stability, reusability, high surface area, suitable morphology and desired band gap [6, 35, 36]. Metal oxide nanomaterials along with advantages have some disadvantages as well such as highly cytotoxic. These nanomaterials can easily enter into the human body via skin, lungs, or intestinal tract due to their small sizes. Inside body, they penetrate into different organs and alter many adverse biological reactions and ultimately affect their tissues [37, 38].

1.12 Applications of Metal Oxides Nanomaterials

Metal oxide nanomaterials found many applications in different fields due to their unique properties. Metal oxide nanomaterials can be used for targeted drug delivery to the infected cells in human body to avoid harmful effects of drug for healthy cells. Metallic nanoparticles have time varying response to external magnetic fields. The

external field transfers energy to a nanoparticle which appears in form of heat. This toxic heat can be used for thermotherapy of tumours [23]. One most common application of metal oxides is photocatalysis. In Photocatalysis, metal oxides utilize light energy to perform various chemical reactions. These reactions can be used for overcoming water pollution and enhancing energy production. The basic mechanism for photocatalysis by metal oxide is discussed below in next section.

1.12.1 Photocatalysis

Photocatalysis is used for detoxification of air, water pollutants degradation and water splitting processes. The word "Photocatalysis" is combination of two words. *Photo* means light while *Catalysis* is the process that increases rate of chemical reaction using catalyst. Photocatalysis is the name for a process in which light is used to activate a substance that enhances the rate of chemical process without self-involving. The material used for this purpose is known as photocatalyst.

Chlorophyll is a naturally existing most important photocatalyst in plants which converts CO_2 and H_2O into glucose in the presence of sun light. Photocatalyst can be synthesized in laboratory. TiO_2, MgO_2 and WO_3 are the examples of some well-known artificial photocatalysts. It reacts with complex organic dyes and yields CO_2 and H_2O in presence of light. That is why TiO_2, MgO_2 and WO_3 are used to degrade the organic dyes in water. An efficient photocatalyst material is one that possesses the following properties [39],

1. Large surface to volume ratio (*Provide more surface area for chemical reaction*)
2. Small band gap (*Utilize the visible spectrum of solar light*).
3. Stability (*Withstand to harsh operating environment*).

1.12.1.1 General Mechanism

When photocatalyst is added to the Water polluted by some dye. It reacts with the dye and decomposes the dye into environment friendly components through mechanism called photosensitised reactions. The photosensitised reactions can be divided into two categories [40],

1. Energy transfer photosensitised reaction

The general mechanism for energy transfer photosensitised reaction are given as,

$$C + hv \rightarrow C^*$$

$$C^* + S \rightarrow S^* + C$$

$$S^* \rightarrow P$$

In this reaction, photocatalyst transfer energy to form an activated reactant state of interest to oxidise easily than its ground state. During the processes, first light interact with photocatalyst (C) which yield excited photocatalyst (C*). The excited photocatalyst then transfer its energy to reactant (S), to make activated reactant (S*). this activated reactant further produces the final product (P). These processes are depicted with the help of fig 1.15.

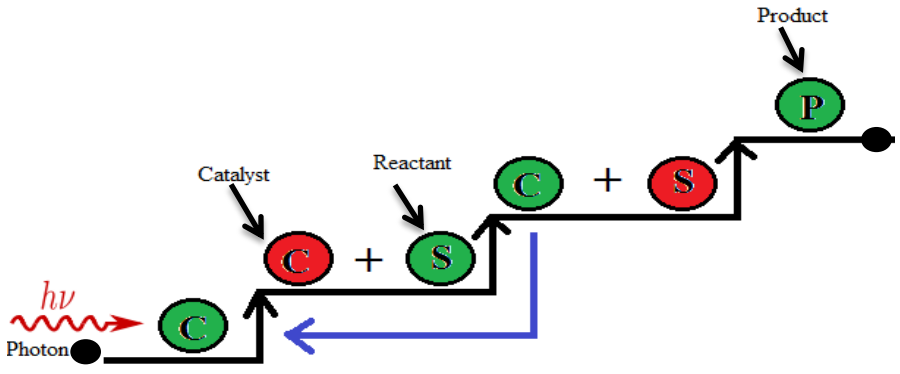

Figure 1.15: Energy transfer mechanism of photocatalyst.

2. Electron transfer photosensitised reaction

The general mechanism for electron transfer photosensitised reaction are given as

$$C + hv \rightarrow C^*$$

$$C^* + S \rightarrow S^- + C^+$$

$$S^- \rightarrow P^-$$

$$P^- + C^+ \rightarrow P + C$$

In these type reactions photocatalyst can work as an electron donor or accepter by absorbing light. The mechanism of this reaction starts from absorbing radiation by catalyst (C), which excites the valence electrons in catalyst (C). In next step, catalyst (C^*) transfer excited electron to reactant (S) and form negatively charged reactant (S^-). Further in process reactant (S^-) yields negatively charged product (P^-). In last step, the negatively charged product reacts with positively charged catalyst where they neutralise each other. This mechanism is shown in fig 1.16.

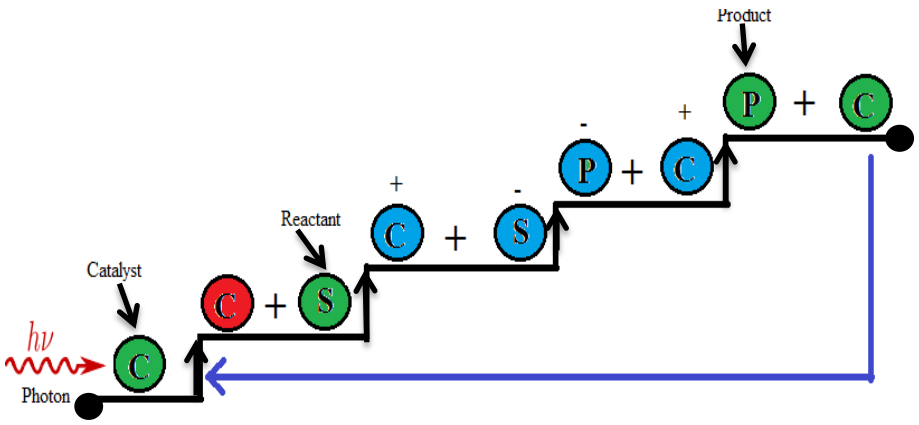

Figure 1.16: Electron transfer mechanism of photocatalyst.

1.13 Tungsten Oxide at Nanoscale

Tungsten oxide (WO_3) belongs to metal oxide, where Tungsten lies in transition metals (d-block) of periodic table. It has large applications in different fields. For the first time in 17^{th} century, the synthesis of WO_3 were started [41]. New inventions in nanotechnologies further make WO_3 more prominent material for different applications. The synthesis of WO_3 nanostructures improves its performance and functionality compare to that in bulk. In bulk, its surface to volume ratio is not large while at nanoscale ratio becomes effectively large and makes WO_3 to provide more surface area for physical as well as chemical reactions. The advantages of nanostructured WO_3 over bulk are given as below,

- Large surface to volume ratio which enhances its reactivity
- High sensitive surface energy that tuning the material properties
- Quantum confinement, which effect significantly electronic band structural, optical and charge transport properties

Nanostructured WO_3 gets high attention of many researchers, for its versatile and unique characteristics. It is one of most investigated functional transition metal oxide in various research fields. WO_3 nanostructure has an excellent electrochromic and gasochromic properties. The same material in addition has good photocatalytic and sensing properties.

1.13.1 Crystal structures

WO_3 forms different phases by corner sharing such as monoclinic-II (ε-WO_3), triclinic (δ-WO_3), monoclinic-I (γ-WO_3), orthorhombic (β-WO_3), tetragonal (α-WO_3) and cubic WO_3. Experimentally, The cubic WO_3 is not observed commonly [42]. The observed lattice constant for each phase of WO_3 is given in Table 1.2 [43-45].

Table 1.2: Lattice constant data for different WO_3 crystal phases.

Crystal phase	a (nm)	B (nm)	C (nm)
ε-WO_3	0.737	0.737	0.766
δ-WO_3	0.730	0.752	0.768
γ-WO_3	0.730	0.754	0.769
β-WO_3	0.738	0.751	0.384
α-WO_3	0.525	N/A	0.391
Cubic-WO_3	0.384	N/A	N/A

In bulk WO_3, transition among above phases occurs in order as shown in fig 1.17 [46, 47].

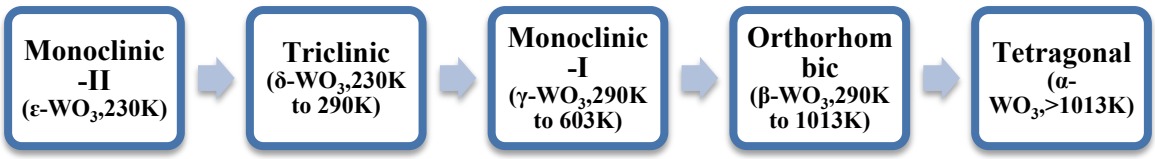

Figure 1.17: Sequence for phase transition of WO_3.

Monoclinic (γ-WO_3) is the only observed stable phase at room temperature. Rarely triclinic (δ-WO_3) is also observed at room temperature. Furthermore WO_3 can exist in hexagonal crystal structure (h-WO_3) which was for the first time observed by Gerand et al in 1979 [48]. The hexagonal crystal can be obtained by slow dehydration of tungstate. However, this hexagonal crystal phase is metastable and transformed into monoclinic phase when heated at 752K. The reported lattice constants for h-WO_3 are a = 0.729 nm and c = 0.389 nm.

In nanostructured WO_3, the phase transitions are quite complex and depend greatly on the materials morphology [49].

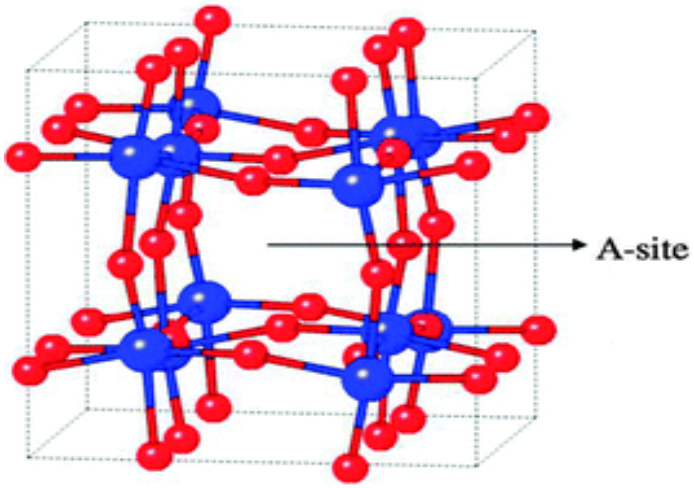

Figure 1.18: Monoclinic structure of WO_3 a) Red spheres represent "O" b) Blue spheres represent "W" [50].

In fig1.18, the monoclinic structure of WO_3 is shown. Most of WO_3 exist in this crystal structure at room temperature in which each W atom is surrounded by six Oxygen atoms in octahedral arrangement.

1.13.2 Band gap energy

In any material valence and conduction bands play very important role in defining its different physical properties like electrical, optical, chemical etc. Electronic states that are located below the valence band don't take part in electrical, chemical and physical processes. Material can be classified into conductor, insulator and semiconductor on the bases of their band gap energy "E_g". WO_3 is an n-type semiconductor, whose band gap value ranges from 2.5 eV to 3.2 eV. Amorphous WO_3 possess relatively large "E_g" of the order of 3.2 eV.

Generally it is found that in nanostructured material, band gap increases with decreasing the size of grain [51]. As a result of increasing "E_g" a blue shift is observed in optical absorption.it is known that this shift is attributed to quantum confinement effect [52]. Gullapalli et al [51], prepared thin films of WO_3 with various thickness using radio magnetron sputtering method. Through this technique, he was able to grow crystals ranging from 9 nm to 50 nm at different temperature. He reported that with reducing the crystallite size significant blue shift in spectrum is observed due to tuning in band gap.

1.13.3 Optical properties

The band gap of WO_3 nanomaterial can be fined using relation.

$$(h\nu)\alpha \propto (h\nu - Eg)^{\eta} \qquad (1.6)$$

In equation 1.6, the "hv" is photon energy while exponent "η" denotes the nature of transition. The calculated band gap for WO_3 nanostructures using equation 1.6 is shown graphically in fig 1.19.

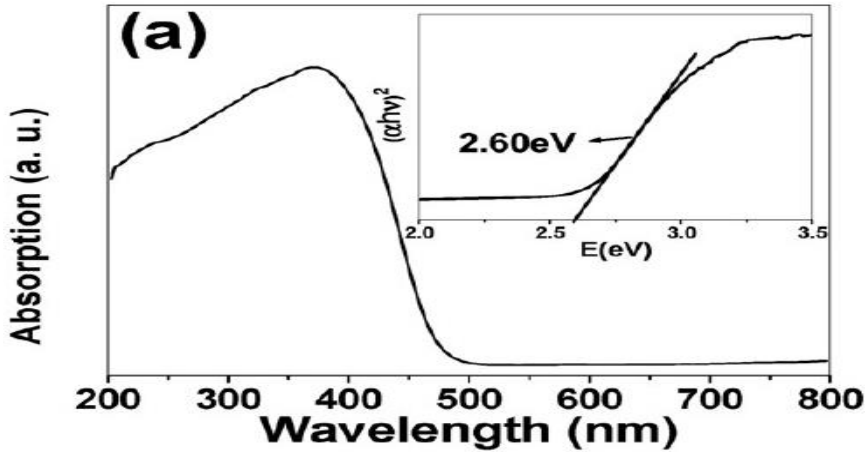

Figure 1.19: UV-Vis spectra of WO_3 nanomaterials, inset graph shows the band gap of WO_3 [53].

1.14 Applications of WO_3 Nanomaterials

In synthesis of WO_3 nanostructures due to control on their size and morphology, researcher founds interesting applications in different fields. One interesting application of WO_3 is the effect of changing colour using external applied voltage is called electrochromism. In smart windows and displays, WO_3 based electrochromic (EC) devices are used because they consume low power and have long stability. When an external voltage is applied, it drives ions (H^+,Li^+) into WO_3 and intercalate, which cause chromic effect [54]. Recently researchers design a self-sustainable WO_3 based EC device called photoelectrochromic (PEC) cell which needs no external power for chromic process. A lot of research is also going on WO_3 based dye sensitized solar cells (DSSC). WO_3 is considered to be alternative of TiO_2 for electronic and catalytic properties.

1.14.1 Visible light driven photocatalytic activity.

Tungsten oxide nanostructures can be efficiently used for different photochemical (PC) reactions. These PC reactions can be utilized to perform dye degradation or water splitting processes under UV light. In dye degradation, WO_3 absorbs light energy to produce "OH" and "$^{\bullet}O_2^-$" ions. Then these ions react with dye and degrade it into H_2O and CO_2 components. While in water splitting processes the absorbed light energy in WO_3 use for decomposing the water into "H_2" and "O_2". In these two types of reactions the first is used for organic pollutant degradation in waste water and the second is used for harvesting solar energy.

1.15 Effect of doping on WO_3

Pure WO_3 nanomaterials have limited commercial applications due to wide band gap and less reactive nature. In order to make it more industrious, various strategies have

been adopted by researchers in literature. Among these methods, doping has primary importance in tailoring WO_3 physical and chemical properties for various practical applications.

Different metals and non-metals can be doped in WO_3 nanostructures via simple co-precipitation, sol-gel and hydrothermal synthesis methods. Literature on WO_3 shows that, doping of transition and non-transition metals in WO_3 nanostructures enhance its physical characteristics. The doping of Li and Na which intercalates in WO_3 nanostructures induces significant chromic effects. The combination of metal oxides such as TiO_2, MnO_2, Co_2O_4 and LiO_2 with WO_3 improves the electrical conductivity of WO_3 nanostructures [39]. It is found that when CeO_2 is combine with WO_3, it increase the gas sensing property of WO_3 nanomaterial by increasing the surface area of grain. Furthermore doping Ce, Pt and Mn in WO_3 nanostructures decrease the band gap of host material which increases the Photocatalytic activity in visible region.

Chapter No. 2

SYNTHESIS TECHNIQUES

The aim of this chapter is to discuss the preparation of undoped and Cerium doped Tungsten oxide nanoparticles. There are different techniques applied for synthesis of WO_3 nanoparticles like vapour and liquid based methods. The synthesis method greatly affects the morphology of prepared nanostructures. Most of time we interests in that technique through which we have best control on morphology of nanostructures, easy to conduct and low in cost.

2.1 Synthesis approaches

For the formation of nanostructures two routes are followed.

- Top-down approach
- Bottom-up approach

In first type, one takes start from bulk material and reduces to desire nanoscale while in second type starts collection from atomic scale and reach to the required nanoscale. Both of these techniques are the reverse of each other and play important role in nanotechnology. Ball milling and nanolithography are the examples of top-down method while sol-gel, co-precipitate, electro deposition, physical and chemical vapour deposition are examples of bottom-up method. Bottom-up approach has advantage over Top-down approach due to its low cast and high control on size and shape. The schematic diagram of both processes is shown in figure 2.1.

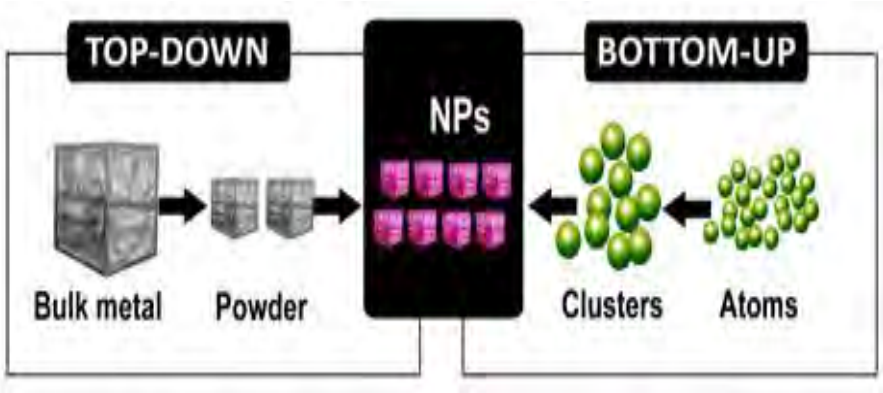

Figure 2.1: Top-down and Bottom-up approaches.

2.2 Co-precipitation technique

It is the simplest, cost effective and environmental friendly method among the chemical techniques for the preparation of WO_3 nanoparticles. It consumes very less time in preparation of ultra-fine nanoparticles. The special advantage of co-precipitation method over all other synthesis method is that it produces the material at very low temperature. Following this method, ultra-high purity (99.99%) materials can synthesis with control physical, mechanical and chemical properties.

2.3 Synthesis of undoped WO_3 nanoparticles

WO_3 exhibits ReO_3 type known structure which consists of layers that containing distorted corner-shared WO_6 octahedra [55].

The formation of WO_3 nanostructure consists of following three steps,

- Formation of Tungstic acid (H_2WO_4)
- Formation of Tungsten oxide clusters by decomposition of (H_2WO_4)
- WO_3 crystal growth

In following Table the detail of chemicals with their formula used in synthesis of WO_3 nanoparticles is given in Table 2.1.

Table 2.1: Chemicals, used in synthesis of $Ce_xW_{1-x}O_3$ nanoparticles.

Chemical Name	Formula	Molecular weight(g/mol)	Supplier
Sodium Tungstate Dehydrate	$Na_2WO_4.2H_2O$	329.86	Sigma-Aldrich
Cerium Nitrate	$Ce(NO_3)_3.6H_2O$	434.22	Sigma-Aldrich
Sodium Chloride	NaCl	58.44	Sigma-Aldrich
Hydrochloric Acid	HCl	36.46	Sigma-Aldrich

Synthesis Procedure: WO_3 nanoparticles were synthesised using co-precipitation method. The starting precursors were 99.99% pure. First of all the measured amount of sodium tungstate dihydrate dissolved in 50ml of distilled water to make 0.1M solution. The homogeneous solution formed after stirring for 10 minutes. Then a measured amount of NaCl was added to the solution as structure directing agent (SDA) and stirred for next 10 minutes. 3M HCl solution start adding drop wise under vigorous stirring until pH value reached to one. The addition of HCl solution result a cloudy mixture. The mixture with pH=1 leaved for 1houre stirring at 80^oC. At the end yellow a type precursor was obtained. The obtained precursor was washed three times with distil water using centrifuge machine at 3000 rpm. The collected residue was dried in oven at 80^oC for 16 hours. Finally the dried sample annealed in furnace for two hours at 600^oC.

The chemical reactions for upper mention process are given below.

$$Na_2WO_4 + 2HCl \longrightarrow 2NaCl + H_2WO_4$$

$$H_2WO_4 \longrightarrow WO_3 + H_2O$$

2.4 Synthesis of Cerium doped WO_3 nanomaterials

The same process was repeated as for in the synthesis of WO_3 nanoparticles but here the concentration of Sodium Tungstate Dihydrate and Cerium Nitrate Hexahydrate was balanced as given below,

- **molar solution of Sodium Tungstate Dihydrate**

$Na_2WO_4.2H_2O$ (Molar mass) = 329.86 g/mole

The amount of solute for 0.1M.

$Na_2WO_4.2H_2O$ (50 ml) = (0.1 × 329.86 × 50) / 1000 = **1.649 g**

- **molar solution of Cerium Nitrate Hexahydrate**

$Ce(NO_3)_3.6H_2O$ (Molar mass) = 434.22 g/mole

The amount of solute for 0.1M.

$Ce(NO_3)_3.6H_2O$ (50 ml) = (0.1 × 434.22 × 50) /1000 = **2.171 g**

- **$Ce_xW_{1-x}O_3$ Compositions**
  - **For x= 0.01, $Ce_{0.01}W_{0.99}O_3$**

The amount of sodium tungstate for given percentage

(99%) $Na_2WO_4.2H_2O$ = 0.99 × 1.649g = **1.632 g**

The amount of Cerium nitrate hexa-hydrate for given percentage

(1%) $Ce(NO_3)_3.6H_2O$ = 0.01 × 2.171 g = **0.021 g**

- **For x= 0.03, $Ce_{0.03}W_{0.97}O_3$**

The amount of sodium tungstate for given percentage

(99%) $Na_2WO_4.2H_2O$ = 0.97 × 1.649 g = **1.599 g**

The amount of Cerium nitrate hexa-hydrate for given percentage

(1%) $Ce(NO_3)_3.6H_2O$ = 0.03 × 2.171 g = **0.065 g**

- **For x= 0.05, $Ce_{0.05}W_{0.95}O_3$**

The amount of sodium tungstate for given percentage

(95%) $Na_2WO_4.2H_2O$ = 0.95 × 1.649 g = **1.566 g**

The amount of Cerium nitrate hexa-hydrate for given percentage

(5%) $Ce(NO_3)_3.6H_2O$ = 0.05 × 2.171 g = **0.108 g**

- **For x=0.08, $Ce_{0.08}W_{0.92}O_3$**

The amount of sodium tungstate for given percentage

(92%) $Na_2WO_4.2H_2O$ = 0.92 × 1.649 g = **1.517 g**

The amount of Cerium nitrate hexa-hydrate for given percentage

(8%) $Ce(NO_3)_3.6H_2O$ = 0.08 × 2.171 g = **0.173 g**

- **For x=0.1, $Ce_{0.1}W_{0.9}O_3$**

The amount of sodium tungstate for given percentage

(90%) $Na_2WO_4.2H_2O$ = 0.90 × 1.649 g = **1.484 g**

The amount of Cerium nitrate hexa-hydrate for given percentage

(10%) $Ce(NO_3)_3.6H_2O$ = 0.1 × 2.171 g = **0.217 g**

The net amount of required precursor for each sample is given in Table 2.2.

Table 2.2: Stoichiometric amounts of precursors

Composition	Amount of Precursors	
$Ce_xW_{1-x}O_3$	$Na_2WO_4.\ 2H_2O$	$Ce(NO_3)_3.6H_2O$
WO_3	1.649g	-----
$Ce_{0.01}W_{0.99}O_3$	1.632g	0.021g
$Ce_{0.03}W_{0.97}O_3$	1.599g	0.065g
$Ce_{0.05}W_{0.95}O_3$	1.566g	0.108g
$Ce_{0.08}W_{0.92}O_3$	1.517g	0.173g
$Ce_{0.10}W_{0.90}O_3$	1.484g	0.217g

2.5 Sample annealing

The prepared light green colour powder sample was placed in furnace for annealing at 600^{o}C for two hours. After two hours heat treatment, the colour of product changed from light green to light yellow. This change in colour is due to dehydration of samples.

2.6 The flow chart of Synthesis processes

The flow chart for aforementioned processes is shown in figure 2.2.

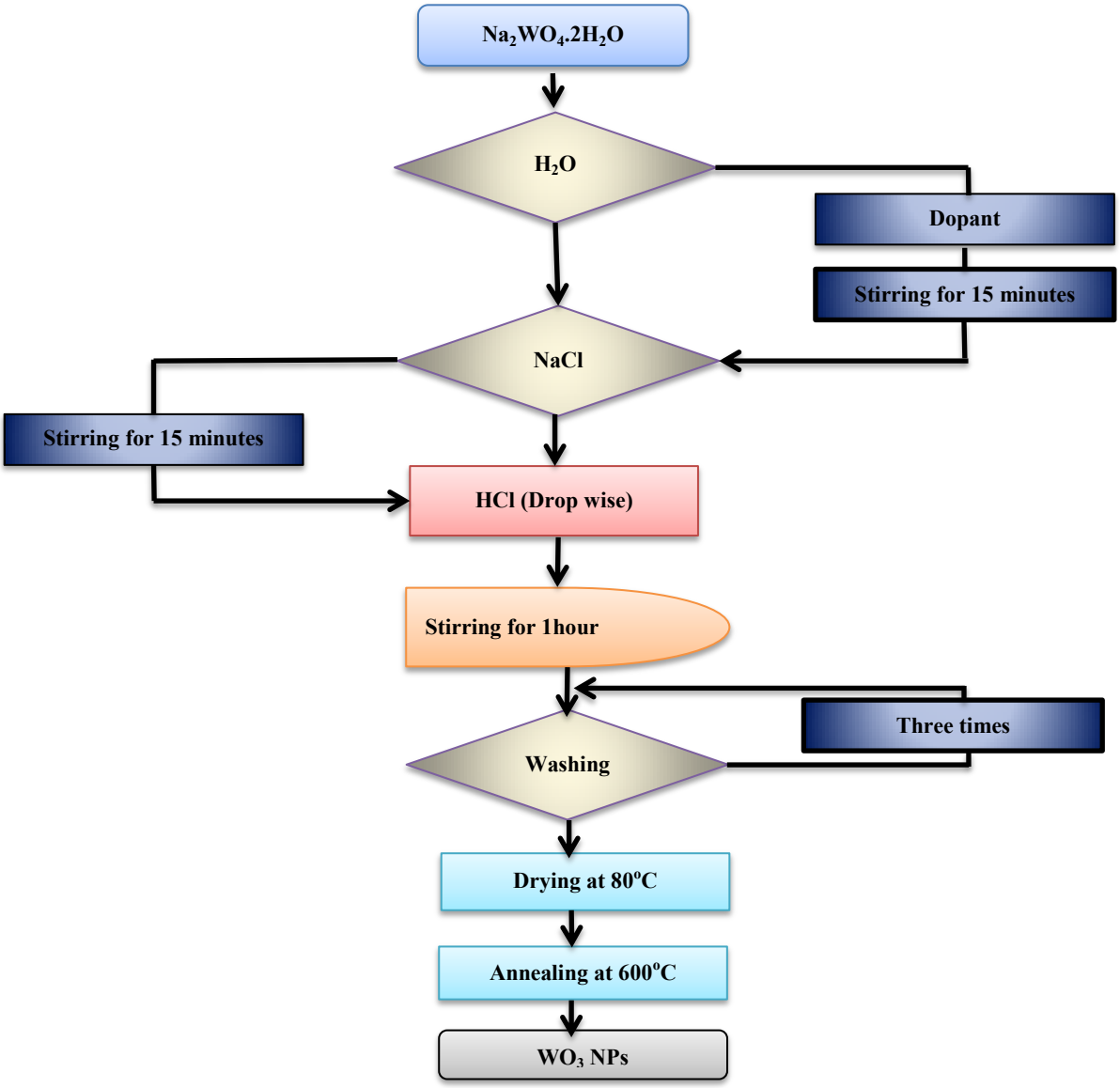

Figure 2.2: Flow chart for synthesis processes.

2.7 Degradation procedure of methylene blue (MB)

The photodegradation of MB has been carried out using 10 mg of WO_3/Ce-WO_3 nanoparticles in 50 ml solution of dye with concentration 1.2 x10^{-5} M/L. Initially the samples were sonicated to get uniform solution, and kept in dark under vigorous stirring

for absorption and desorption. After this process perform UV-visible scan to get degradation results of MB in solution. Then remaining solution was placed in sunlight for 3 hours. For further analyses of photodegradation activity, extract regularly about 3 ml samples after each 30 minutes for UV-visible scan. All samples were tested against degradation of MB by following the same method.

In order to find the degradation percentage, the following equation have been used,

$$\eta = \left(1 - \frac{C}{C_o}\right) \qquad \textbf{(2.1)}$$

In equation (3.1) "η" presents degradation percentage, "C_o" is the initial concentration of dye and "C" is the concentration after certain irradiation time"t".

The rate constant "k" values of all samples find with the help of following equation,

$$\ln\left(\frac{C_o}{C}\right) = kt \qquad \textbf{(2.2)}$$

Where "C_o" is the initial concentration, "C" is the concentration after time t, and "k" is the rate constant.

The flow chart for MB dye degradation process is given in figure 2.3.

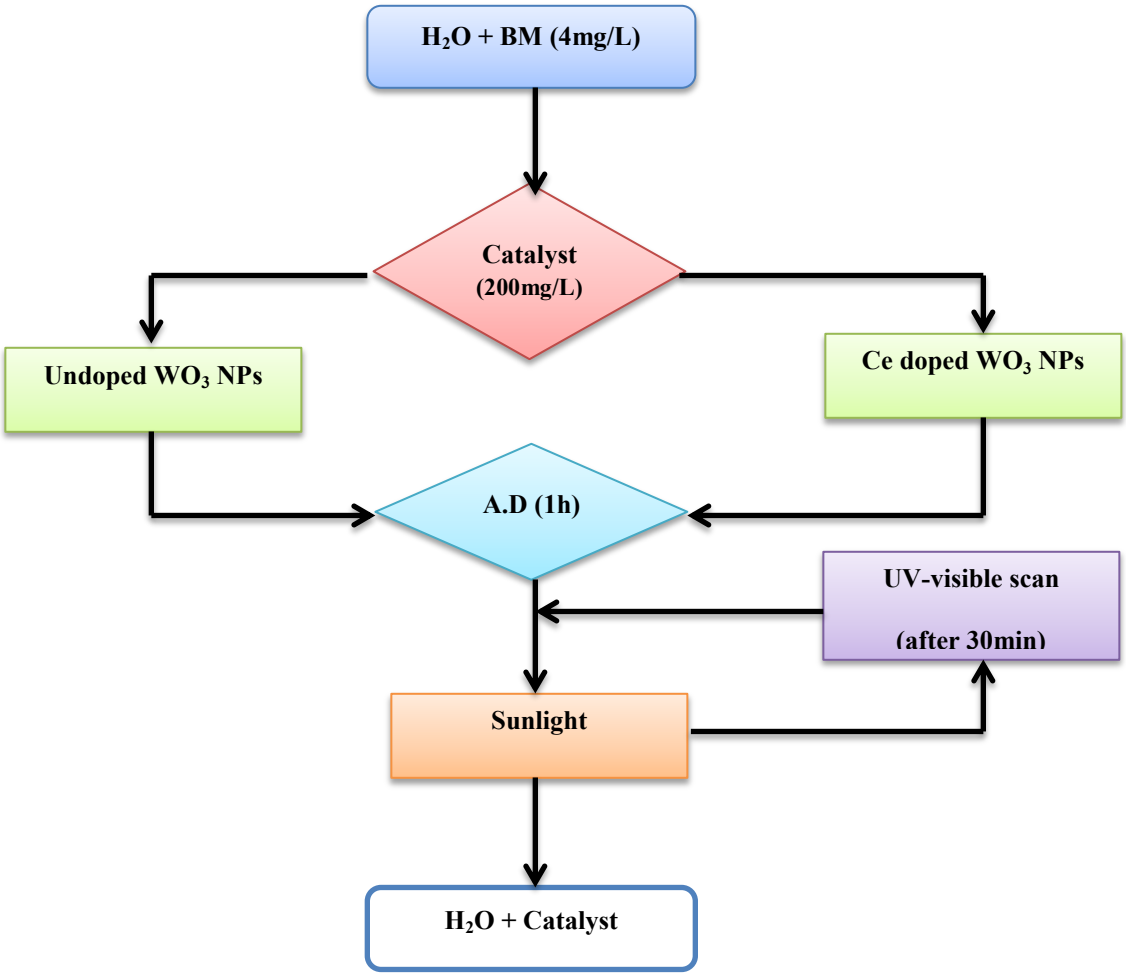

Figure 2.3: Flow chart for photodegradation of MB.

Chapter No. 3

CHARACTERIZATION TECHNIQUES

The aim of research is to synthesis new material with novel properties and excellent functionalities. Following characterization tools have been employed to investigate the properties of prepared nanostructures.

3.1 X-Ray Diffraction (XRD)

X-ray diffraction is one the most common characterization technique which is used all over the world for determining the crystal phases of material. It is non-destructive analytical method and mostly used by material scientists. XRD patterns are considered to be finger print of any material. From XRD, one can get information about crystal structure, spacing between layers, crystallite/particle size, internal stresses and crystal orientation. The working principle of XRD is based on Bragg's law and expressed in equation 3.1.

$$2dsin\theta = n\lambda \quad (3.1)$$

Where "θ" is the scattering angle, "λ" is the wavelength, "n" is the order of diffraction and "d" is the inter planner spacing.

In this process a monochromatic X-ray beam falls on the sample which is under investigation and get scattered by its different planes in different directions. The detector can detect scattered x-rays from sample over large angle. The incoming rays on detector which satisfy Bragg's law and in phase give constructive interference (maxima) pattern while out of phase depict destructive interference (minima). The phenomenon is shown in fig 3.1.

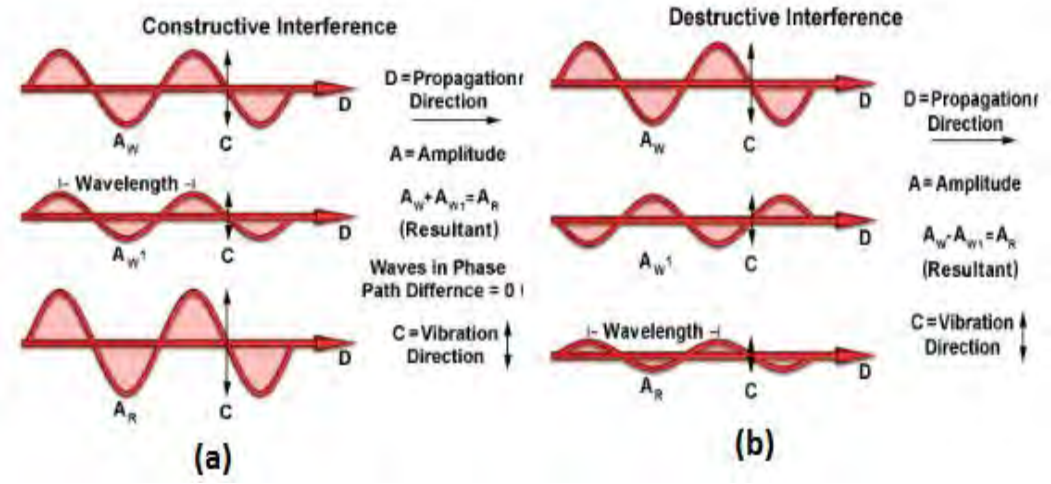

Figure 3.1: a) In phase (constructive interference) b) Out of phase (destructive interference).

Recording these minima and maxima at different angles by detector, generates a diffraction pattern for that sample. The position of Maxima in diffraction pattern varies for different crystalline solids. Short range ordered material (amorphous) gives a broad diffused diffraction pattern.

The typical XRD pattern of Tungsten oxide powder is shown in fig 3.2.

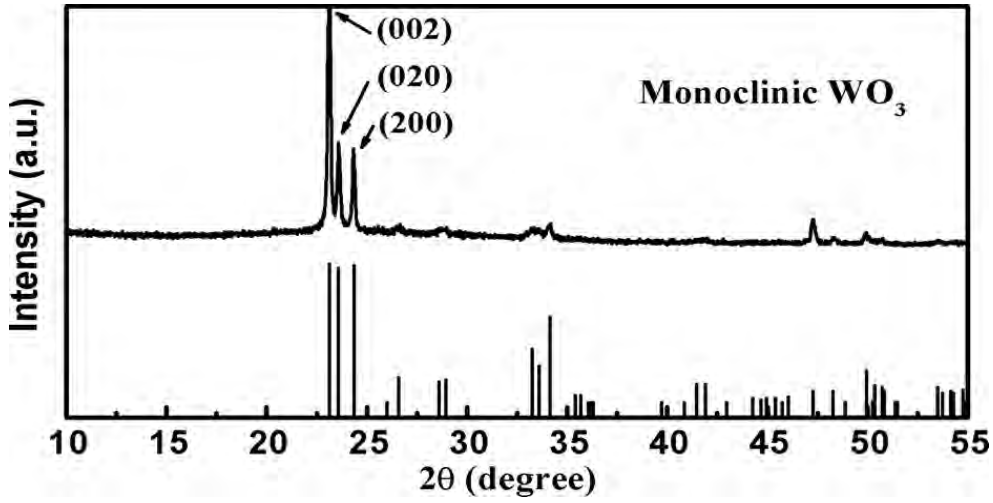

Figure 3.2: XRD pattern of WO_3 nanomaterials.

Using XRD data the crystallite size can be calculated via following equation [56].

$$D = \frac{k\lambda}{\beta cos\theta} \qquad (3.2)$$

This is known as "Scherer formula". Where *"D"* is the crystallite thickness, "λ" is wave length of incident X-ray, "k" is machine constant, "β" is full width at half maximum (FWHM) and "θ" is Bragg's diffraction angle.

3.2 Scanning Electron Microscope (SEM)

Scanning electron microscopy (SEM) creates three dimensional high resolution surface images of sample. In SEM, there is an electron gun which produces electron with high speed. The beam of electrons in SEM condenses by electrostatic or magnetic lenses several times and produce monochromatic condensed beam of electrons. During the operation, the entire system is evacuated to avoid the scattering of electron from any stray air molecules. A set of coils can scan this beam of electron in grid fashion. Different types of interactions take place when beam of electrons incident on the surface of sample as shown in fig 3.3.

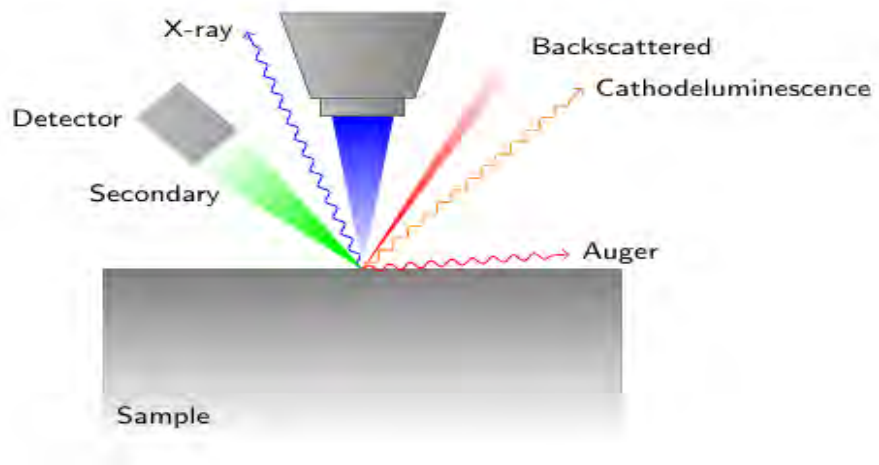

Figure 3.3: Interaction of electron beam with sample surface.

In SEM, during the process of electron beam interaction with sample following different kind of signals are produced from sample.

- **Back scattered electrons**
- **Auger electrons**
- **Secondary electron**
- **Characteristic X-rays**
- **Photons**

In order to record the surface morphology, SEM detector detects only the secondary electrons that are emitted from the surface of sample and carry different information related to surface. The process carried out until whole sample scan is completed. Fig 3.4 depicts the basic components along with its working function.

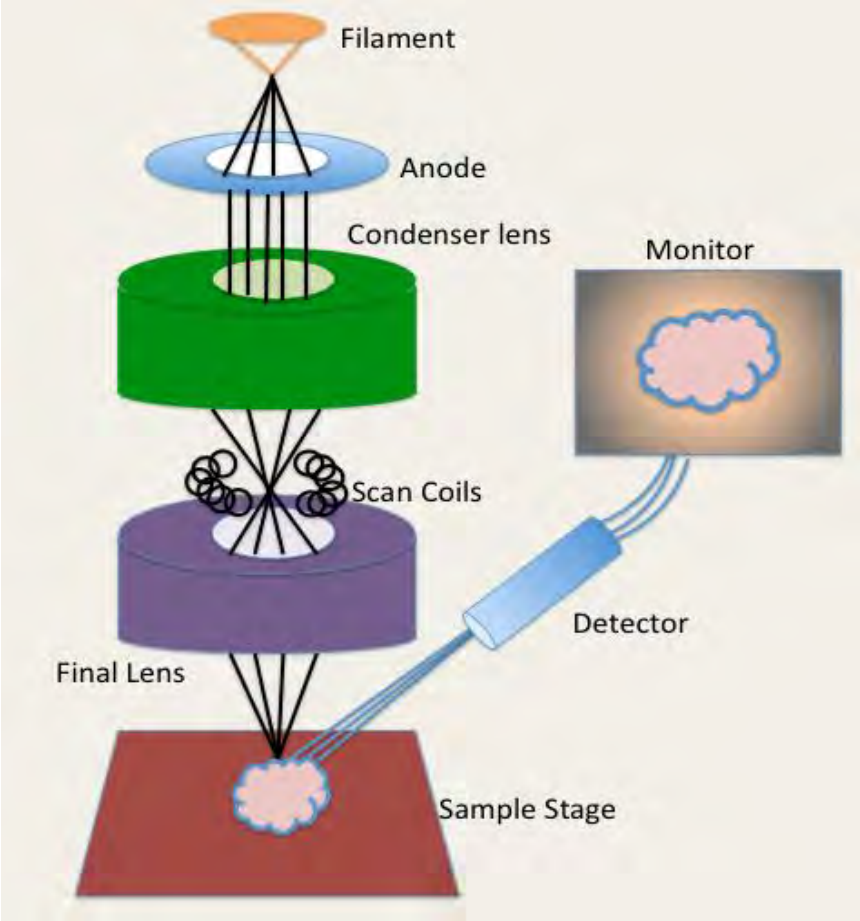

Figure 3.4: Working components of SEM.

Fig 3.5 illustrates the typical morphology scan of WO_3 using SEM.

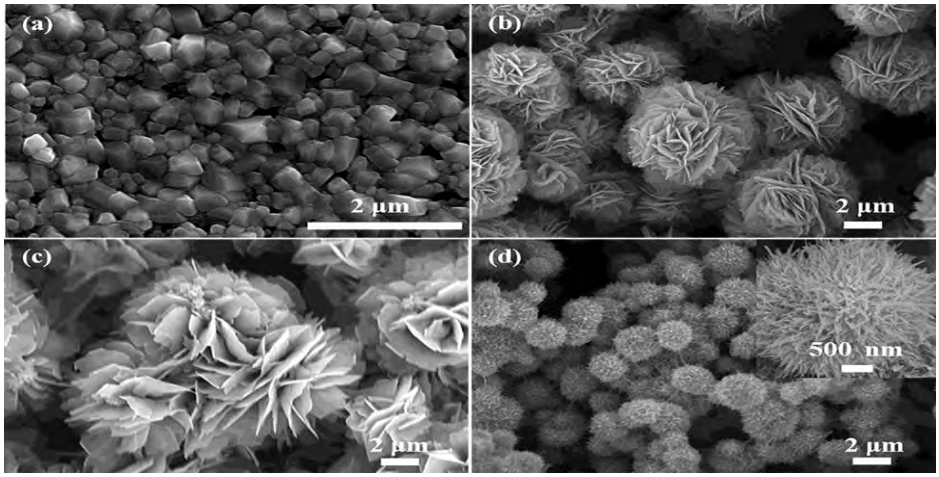

Figure 3.5: SEM images for WO_3 [48].

3.3 FTIR spectroscopy

The energy of a molecule can be resolved into sum of its rotational, vibrational and electronic energy levels. IR spectroscopy deals with the interaction of matter with electromagnetic waves (EMWs) in IR region. The EMWs in IR region can excite a molecule between its rotational and vibrational energy levels. The interaction of EMWs with a molecule high when coincide its energy with its energy levels. IR spectroscopy is considering a very good technique which gives the fingerprint information about the chemical composition of the sample.

3.3.1 Mathematical expression of Fourier Transform

In this process, it is important to know about absorbed and transmitted frequencies. For this, one needs a radiation source which has broad spectral range and a detector which analyse each individual frequency radiation. In FTIR, Fourier Transform uses for fine data analysis. The mathematical expression of Fourier Transform in FTIR is,

$$\boldsymbol{F(\omega) = \int_{-\infty}^{+\infty} f(x) e^{i\omega x}\, dx} \qquad \textbf{(3.3)}$$

And the invers transform is

$$f(x) = \frac{1}{2л}\int_{-\infty}^{+\infty} F(\omega)e^{i\omega x}\, d\omega \qquad (3.4)$$

In equations 3.3 & 3.4 "ω" is the angular frequency, "x" is the optical path difference, "F (ω)" is spectrum and "f(x)" is interferogram.

3.3.2 The Michelson Interferometer

FTIR works on the principle of Michelson Interferometer, the Michelson Interferometer consists of a wide band IR light source, a beam splitter, two mirrors (one movable and one fixed) and a detector. The schematic diagram of Michelson Interferometer is given in fig 3.6.

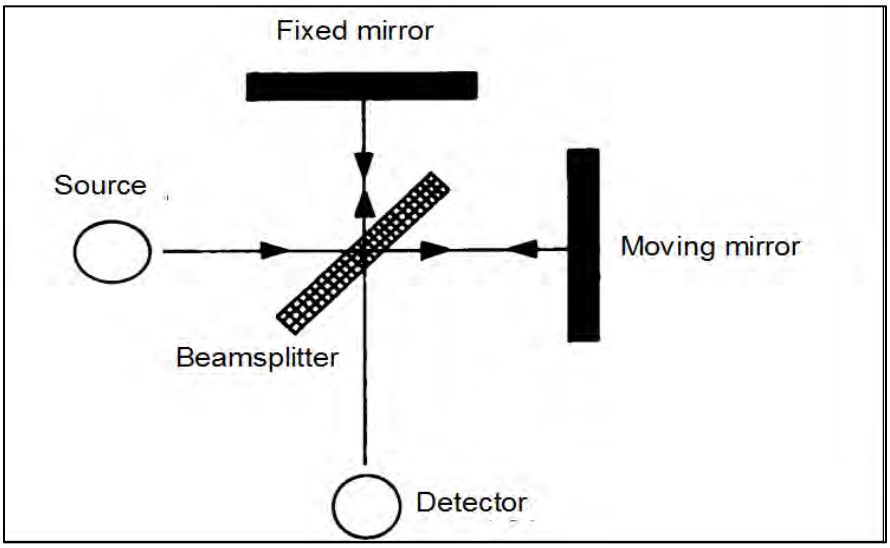

Figure 3.6: Michelson Interferometer.

During the operation, a beam of light from light source enters into spectrometer where the beam splitter splits it into two beams one move towards fixed mirror and the other move towards movable mirror. After reflecting from each mirror two beams move back towards beam splitter where some part of beam transmits in source direction and some

towards the sample. As the beam pass through the sample, it enters the detector. The beam can undergoes constructive and destructive interferences for a specific frequency by adjusting the moving mirror. If the moving mirror allows scanning over a range for that frequency, a sinusoidal signal will be detected. In pattern constructive and destructive interference will lies in alternate fashion which is called interferogram as shown in fig 3.7.

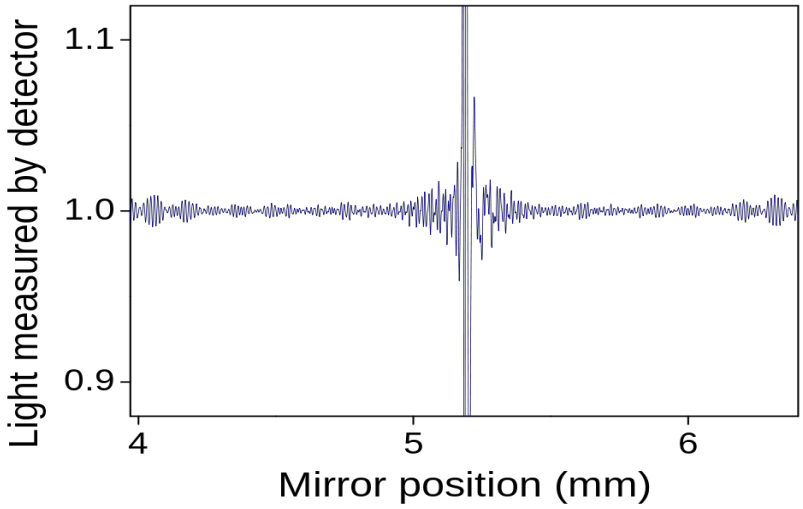

Figure 3.7: interferogram.

In FTIR spectroscopy, interferogram is obtained experimentally while corresponding spectrum of frequency against intensity plot computed by Fourier transform. The typical FTIR spectra of LNT research group is shown in fig 3.8.

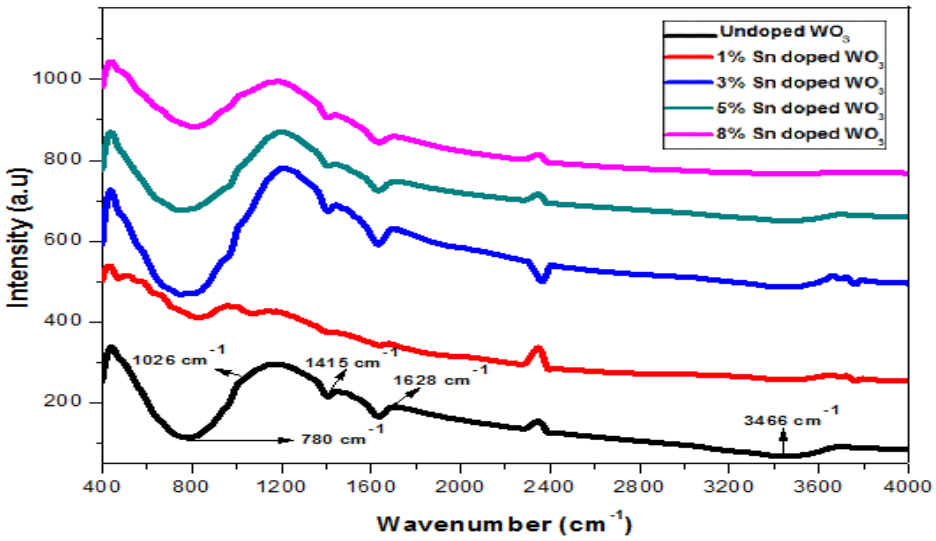

Figure 3.8: FTIR spectra for WO_3 nanostructures [57]

3.4 Raman Spectroscopy

Raman spectroscopy is one of the useful tool to investigate, vibrational modes and defects in nanomaterial. It was introduced by Sir C.V Raman in 1928. In Raman spectroscopy laser light (514nm) is used to study the different vibrational, rotational and other low frequency modes. It helps to fingerprint and study different molecules present in sample. When laser is fall on a material, two kinds of interaction expected,

- Elastic Scattering
- Inelastic Scattering

3.4.1 Elastic scattering

When a photon of certain frequency is absorbed and excites a molecule, it de-excites back to the same basic vibrational state and the light emitted by it has same frequency. This type of interaction is called an elastic or elastic Rayleigh scattering.

3.4.2 Inelastic scattering

In this case the incident photon from light source excites a molecule in sample, which de-excite back not to the same basic vibrational level by emitting light with different frequency. The inelastic scattering is further divided into two types.

- When molecules absorb a photon with high frequency and re-emit photon of low frequency this Raman frequency is called **Stokes**.
- When molecule absorb a photon with low frequency and re-emit high frequency photon this Raman frequency is call **Anti-stokes**.

The mechanism of these elastic and inelastic scattering is shown in fig 3.9.

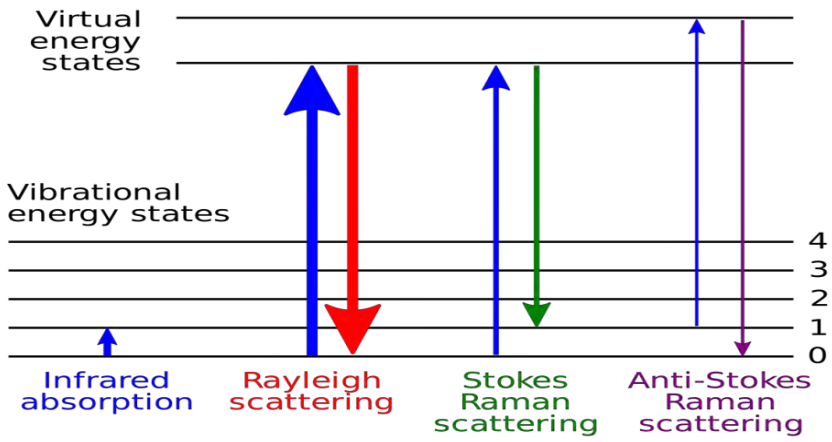

Figure 3.9: Energy-level diagram for Raman spectra.

The typical Raman spectra for WO_3 structure is depicted in fig 3.10, where Roman active modes located at, 255 $cm^{-1}$and 325 cm^{-1}belongs to stretching mode of O-W-O while 690 cm^{-1} and 805 cm^{-1} are liked with bending modes of O-W-O.

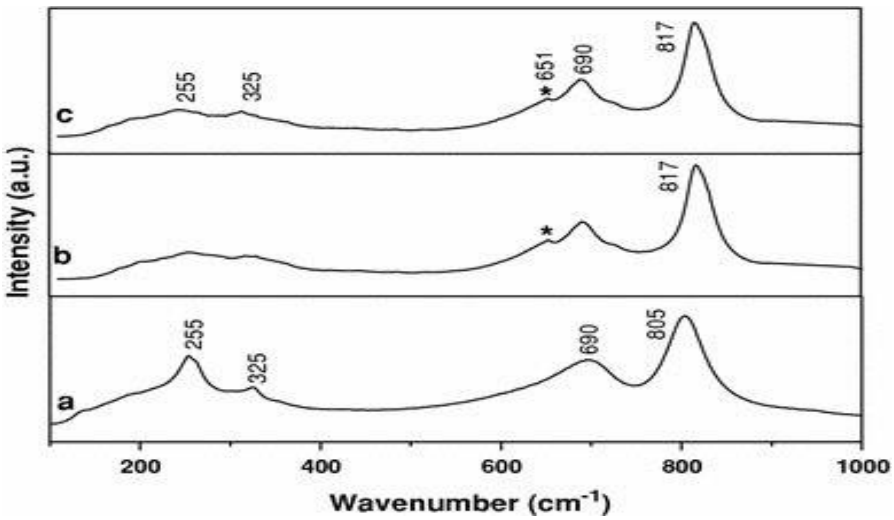

Figure 3.10: Typical Raman spectra for WO_3 [49].

3.5 UV-Visible spectroscopy

UV-Visible spectroscopy is a versatile characterization technique for optical properties. UV-visible spectroscopy works on the analysis of the spectrum of light, which absorbed in a sample. It uses near ultraviolet (UV) region (200-400 nm), visible region (400-700 nm) and near infrared (IR) region (700-1100 nm). Mostly double beam spectrophotometer is used for UV-Visible spectroscopy operation. The spectrometer job is to measure the amount of light being absorbed in sample after illuminating light on it, for each wavelength interval. The spectrometer can operate in the ultraviolet visible spectral range. Spectrometer consists of double monochromatic, double beam ratio recording optical system. The light source of spectrometer is tungsten and deuterium lamps. Its scan range starts from 800 nm to 200 nm with resolution of less than or equal to 0.05 nm for UV-Vis. Moreover scan starts from 800 nm and terminate at 200 nm. In operation, light beam coming from lamp allows to pass through a light filter, to get monochromatic beam of light, which further splits into two equal intensity beams. One of these beams emerges through sample while the other beam passes through the reference substance. The intensity of corresponding beams, coming from the sample and reference

under study, measure and compare using detector. The schematic diagram for UV-Visible spectrophotometer is shown in fig 3.11.

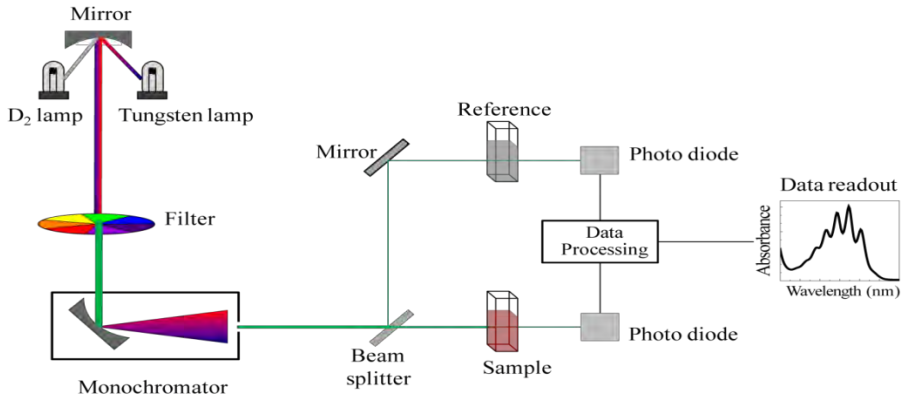

Figure 3.11: UV-Visible spectroscopy, schematic representation

Chapter No. 4

RESULTS AND DISCUSSIONS

4.1 Structural Characteristics

The crystal structures have been investigated using XRD at room temperature for all annealed samples and shown in fig 4.1. The concentration of Ce dopant in WO_3 host matrix have been varied as 0%, 1%, 3%, 5%, 8% and 10% at the time of different sample preparation. In fig 4.1, undoped WO_3 nanoparticles prepared by chemical wet method give clear and sharp peaks at 23.109°, 23.579° and 24.336° for planes (002), (020) and (200) respectively. These results confirm the formation of monoclinic (γ-WO_3) crystal structure according to JCPDS card number 43-1035.

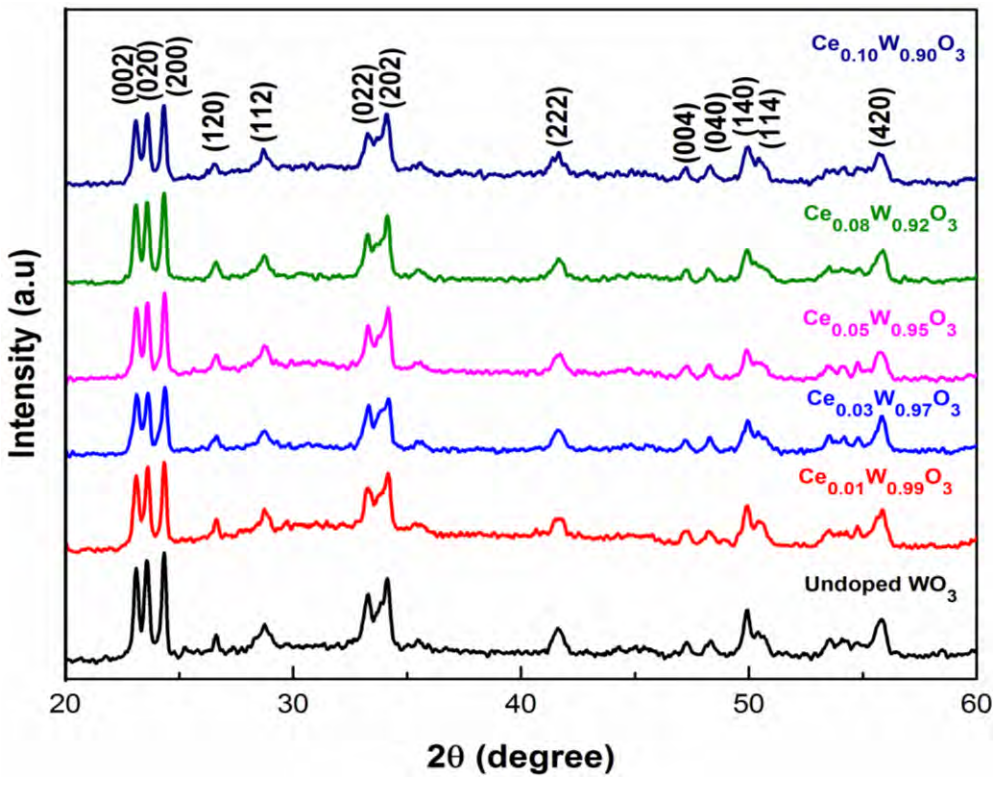

Figure 4.1: XRD patterns of undoped and Ce doped WO_3 nanoparticles.

It can be observed in patterns that the addition of Ce in WO_3 nanoparticles causes slight shift in XRD peaks. According to fig 4.2, the peaks for (002) and (200) planes have shift towards low angle with Ce doping in to WO_3 nanoparticles while a small shift is noticed toward larger angle in (020) and (200) plane peak for 3% Ce doped WO_3 nanoparticles.

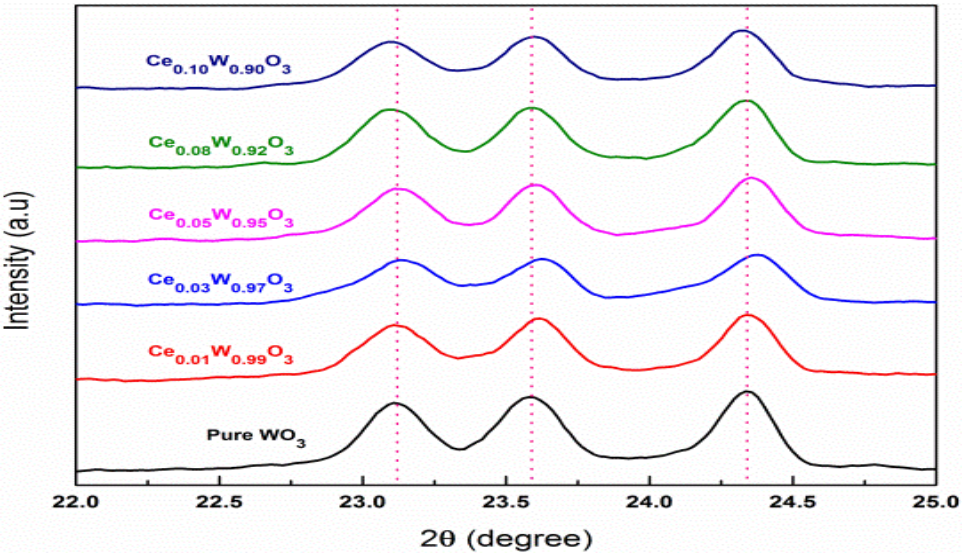

Figure 4.2: XRD prominent peaks of undoped and Ce doped WO_3 nanoparticles.

These shifts in XRD peaks indicate the variation in lattice constants caused by change in ionic radii of host W^{6+}(0.58 Å) and dopant Ce^{4+} (0.97 Å). There is no single extra peak observed for all doped samples which confirm single phase crystallinity of samples. The XRD patterns clearly present that all prepared samples have monoclinic (γ-WO_3) crystal structure.

4.1.1 Average crystallite size

The crystallite size of prepared WO_3 nanoparticles have been calculated from XRD peaks using Sherrer formula given in equation 3.2.

$$\mathbf{D = \frac{K\lambda}{\beta\cos\theta}} \qquad \textbf{(3.2)}$$

In equation 2.2, the value of K = 0.91 and λ = 1.54 nm. Three prominent peaks (002), (020) and (200) located at 23.13°, 23.61° and 24.35° respectively have been used to find the average crystallite size for undoped and Ce doped WO_3.

Table 4.1: Average crystallite size for undoped and Ce doped WO_3 nanoparticles.

Sample name ($Ce_xW_{1-x}O_3$)	Crystalline size from (002) peak (nm)	Crystalline size from (020) peak (nm)	Crystalline size from (200) peak (nm)	Average crystalline size (nm)
0%	28.5	31.8	36.5	33.8
1%	28.7	33.1	35.9	32.5
3%	24.4	33.6	27.5	28.5
5%	31.3	39.7	36.2	35.7
8%	34.0	37.0	36.6	35.8
10%	29.8	33.4	34.5	32.5

The data in Table 4.1 shows that the average crystallite size of WO_3 nanoparticles vary with Ce doping. The crystallite size first decreases with Ce doping and smallest crystallite size is observed for 3% Ce doped sample then increases with doping more than 3% Ce in WO_3 nanoparticles. The results suggest that grain growth is suppressed with Ce (< 3%) doping into host matrix.

4.1.2 Lattice parameter

The lattice constants “a”, “b” and “c” for monoclinic phase of undoped WO_3 and Ce doped WO_3 have been calculated using XRD data. The lattice constants “a”, “b” and “c” are calculated from (200), (020) and (002) respectively and listed in Table 4.2. All calculated values for lattice constants are in good agreement with reported values in literature.

Table 4.2: Lattice constants value for each sample (Å).

Sample Name ($Ce_xW_{1-x}O_3$)	a (nm)	b (nm)	c (nm)
0%	0.731	0.754	0.769
1%	0.730	0.753	0.769
3%	0.729	0.752	0.768
5%	0.730	0.753	0.769
8%	0.730	0.753	0.769
10%	0.731	0.753	0.769

The variation in lattice constant is graphically presented in figs 4.3 - 4.5.

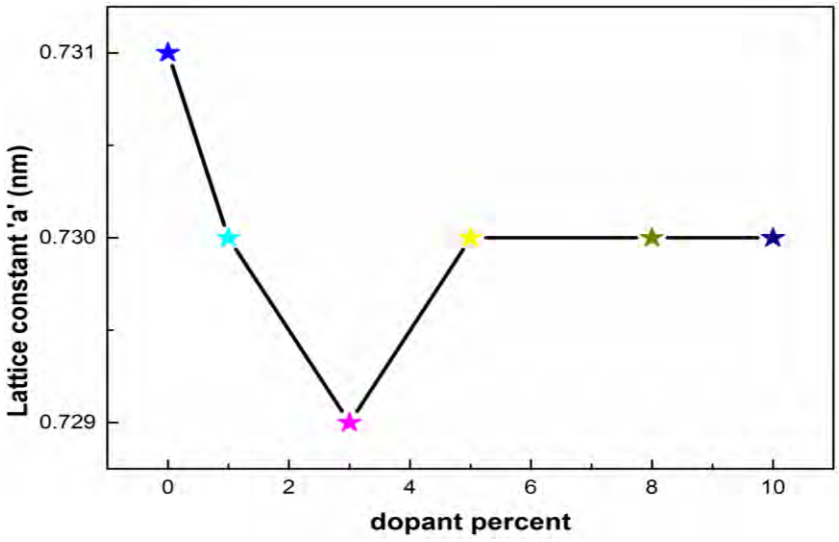

Figure 4.3: Variation in lattice constant "a".

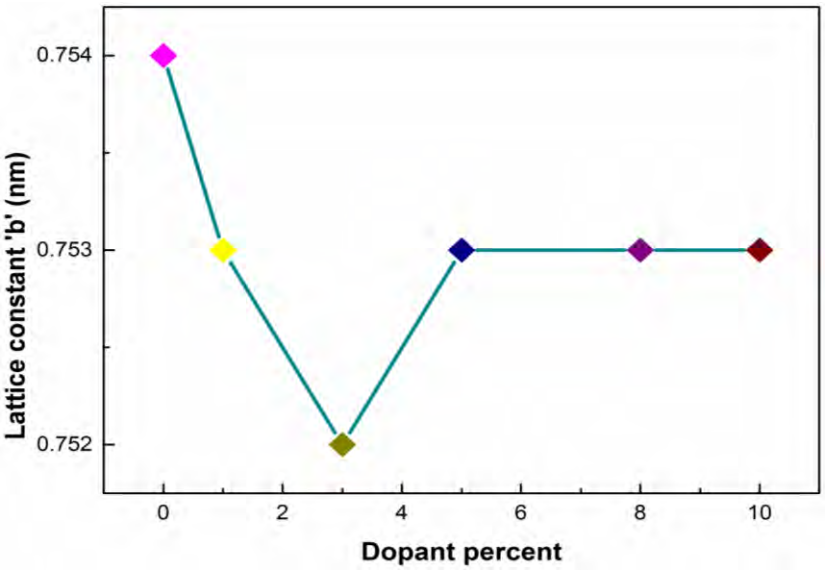

Figure 4.4: Variation in lattice constant "b".

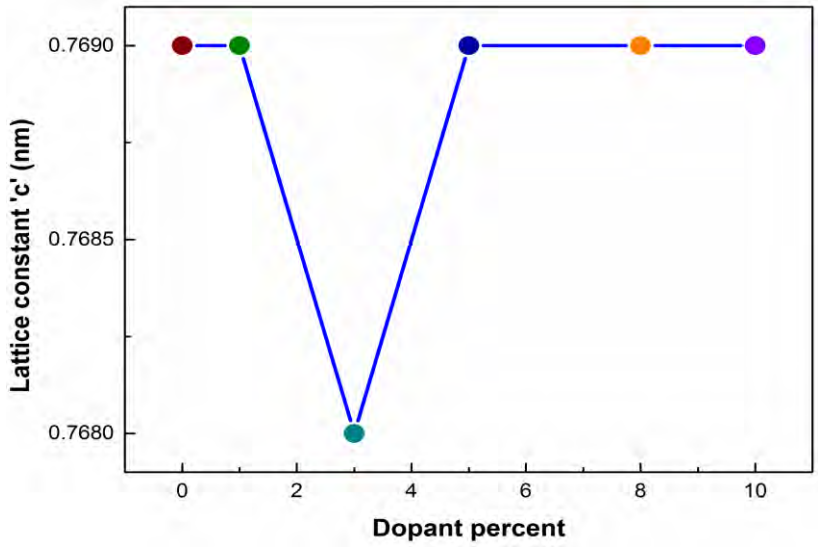

Figure 4.5: Variation in lattice constant "c".

The fig 4.3, 4.4 and 4.5 clearly depicts that lattice constants change with Ce (3%) doping. It indicates that Ce (3%) ions may enter at interstitial site of WO_3 matrix. It is hard for Ce^{4+} ions to replace W^{6+} ions due to large difference in both ionic radii [58].

4.2 Morphological Observations

Scanning electron Microscopy (SEM) has been used to study the surface morphology and sample homogeneity of nanoparticles. The SEM images reveal that synthesised particles have sphere like morphology with size in nanometre range. The prepared nanoparticles in fig 4.6(a-e) confirm their homogeneity.

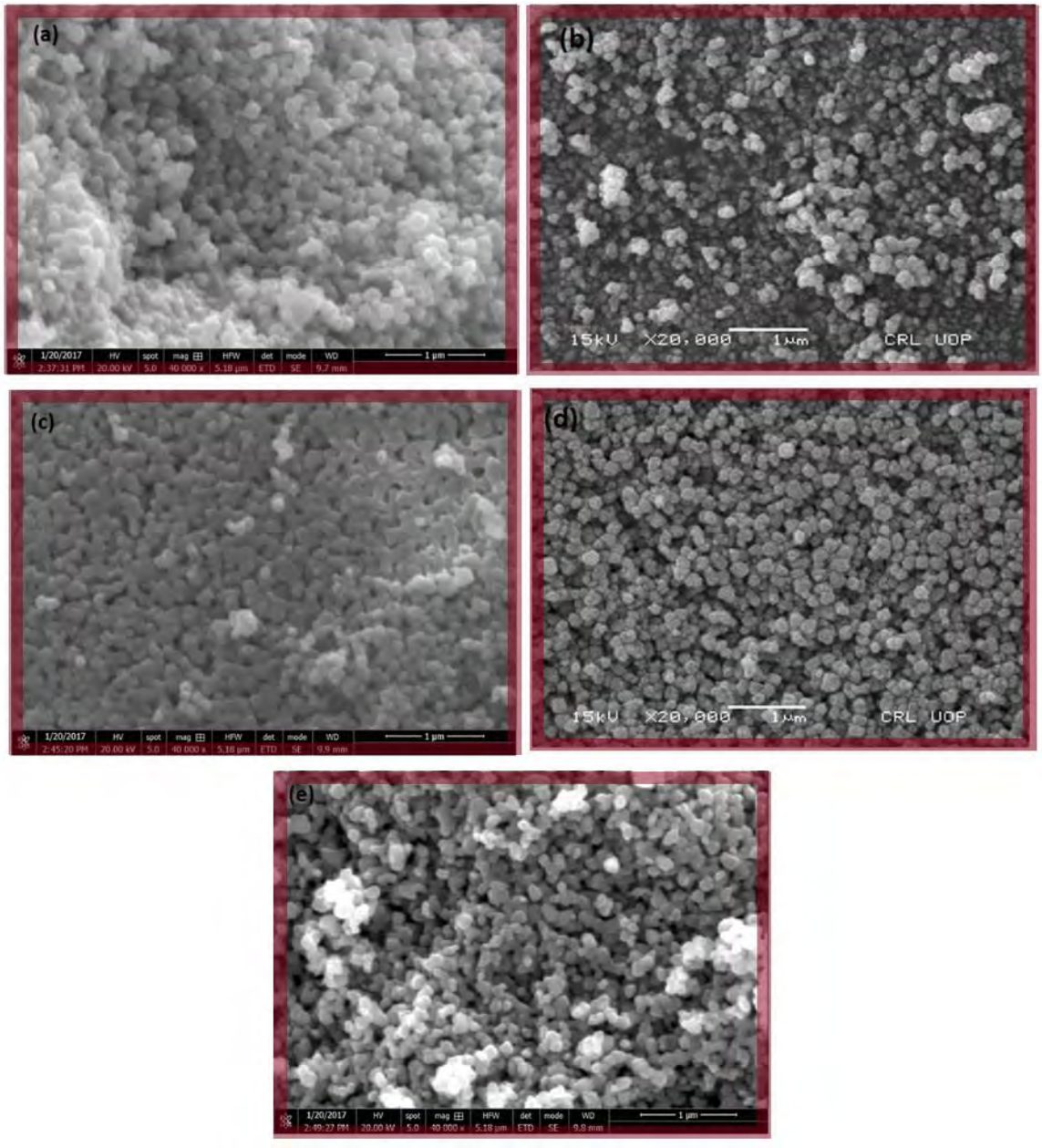

Figure 4.6: SEM images for a) undoped WO_3 b) $Ce_{0.03}W_{0.97}O_3$ c) $Ce_{0.05}W_{0.95}O_3$ b) $Ce_{0.08}W_{0.92}O_3$ e) $Ce_{0.1}W_{0.9}O_3$.

The nanoparticles are well separated in fig 4.6(a, b), and in fig 4.6c the particles seem to be grow in size which is consistent with XRD finding. Where crystallite size increased for 5% Ce doped WO_3 nanoparticles. There are open channels between the surfaces of nanoparticles in fig 4.6(d, e). The SEM analysis shows that the average particle size of samples lies in the range 80-95 nm.

4.3 Vibrational Characterization

The FTIR and Raman spectroscopy are the vibrational spectroscopic techniques use for investigating chemical structure and vibrational modes of nanomaterials. In order to study the surface and defect chemistry of as synthesised samples FTIR and Raman spectra have been recorded at room temperature.

4.3.1 Stretching and bending modes analysis

To examine the chemical quality and surface chemistry of undoped and Ce doped WO_3 nanoparticles, FTIR spectroscopy has been performed. The FTIR spectra for all samples are shown in fig 4.7.

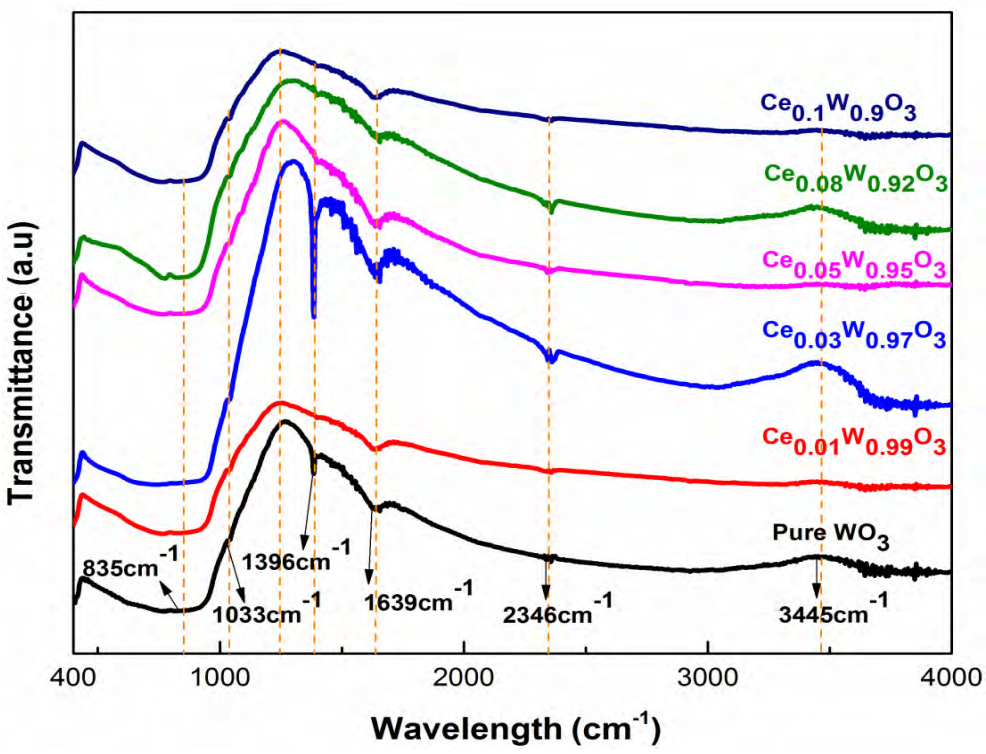

Figure 4.7: FTIR spectra for undoped and Ce doped WO_3 nanostructures.

In fig 4.7 the absorption bands at 1396 cm^{-1} and 1639 cm^{-1} are due to the binding modes of O-H, band at 3445 cm^{-1} belongs to the stretching mode of O-H in water molecule [57]. The large absorption band gap extended from 621 cm^{-1} to 1070 cm^{-1} associated with the stretching modes of O-W-O [59]. The band located at 2346 cm^{-1} is due to atmospheric CO_2 [60].The absence of modes for Ce-O and presence of stretching modes of O-W-O show that Ce is successfully doped into WO_3 host matrix [57].

4.3.2 Vibrational modes investigation

In order to probe further the vibrational properties of synthesised samples, Raman spectroscopy has been carried out. Raman analysis is another characterization technique to check out microstructure properties for undoped and Ce doped WO_3 nanoparticles. Fig 4.8 depicts the Raman spectra of undoped and Ce doped WO_3 nanostructure.

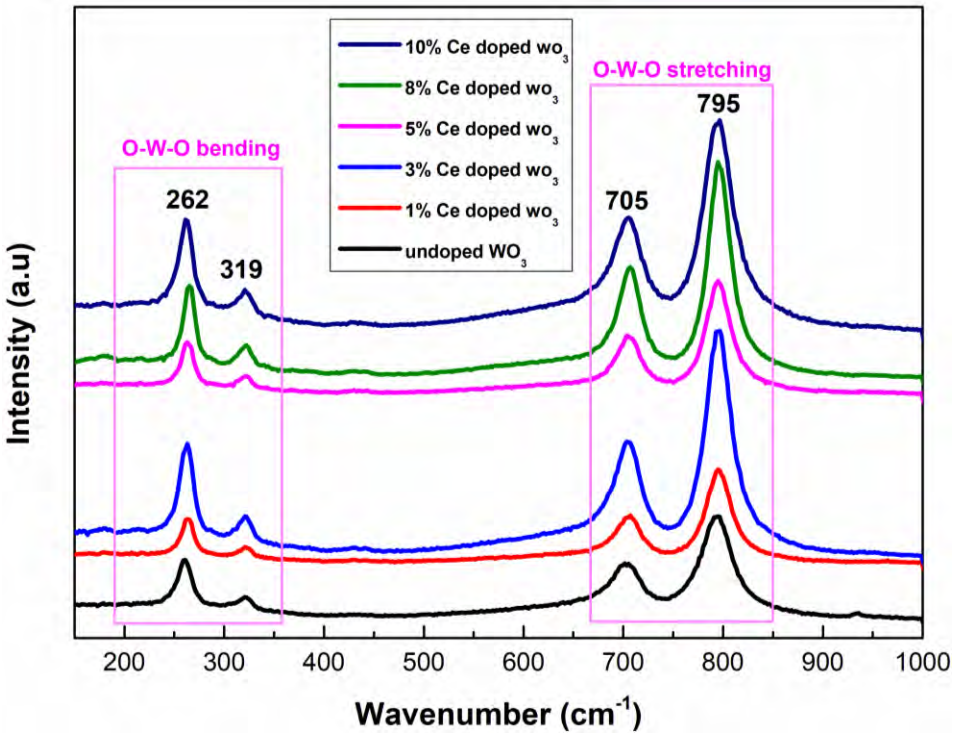

Figure 4.8: Raman spectra for undoped and Ce doped WO_3 nanostructures.

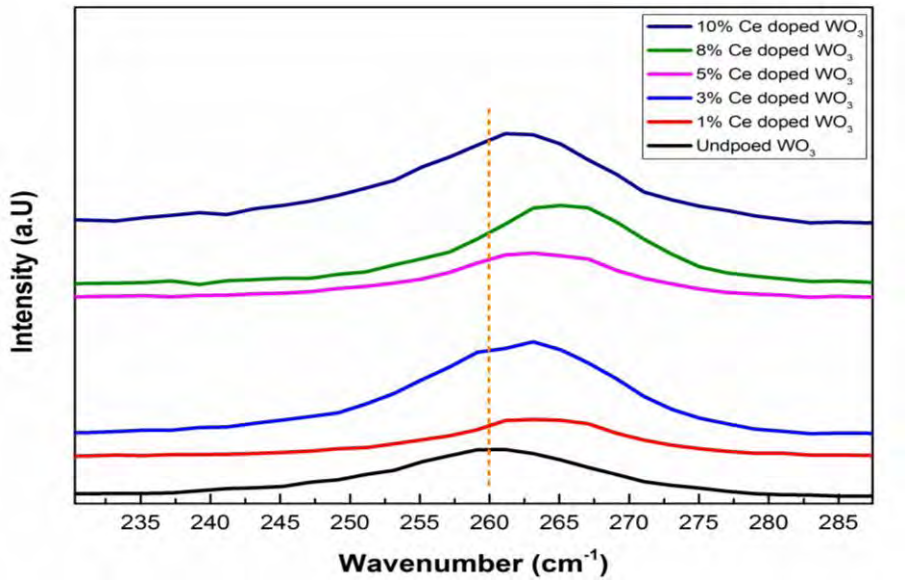

Figure 4.9: Raman peaks shift with Ce doping in WO_3.

In fig 4.8 Raman bands located at 262 & 319 cm^{-1} and that lies at 705 & 795 cm^{-1} linked to binding and stretching vibrational modes of O-W-O respectively. The slight shift in Raman peaks of all Ce doped WO_3 nanoparticles toward higher frequency are observed

in fig 4.9. this shift is attributed due to the presence of oxygen vacancies like defects [61]. The Ce doping in WO_3 nanoparticles alter its Raman active mods intensity. There is no peak observed that link with possible phase CeO_2, which means that according to Raman analysis Ce is successfully dissolved in WO_3 matrix.

4.4 Band gap Studies

For observing the bandgap energy (E_g) between valence and conduction band of undoped and Ce doped WO_3 nanoparticles UV-visible absorption spectroscopy have been studied and spectra is shown in fig 4.10. UV-visible spectroscopy has been performed at room temperature in wavelength range 200-800nm. UV- visible spectra gives us the absorbance value against each wavelength for our samples.

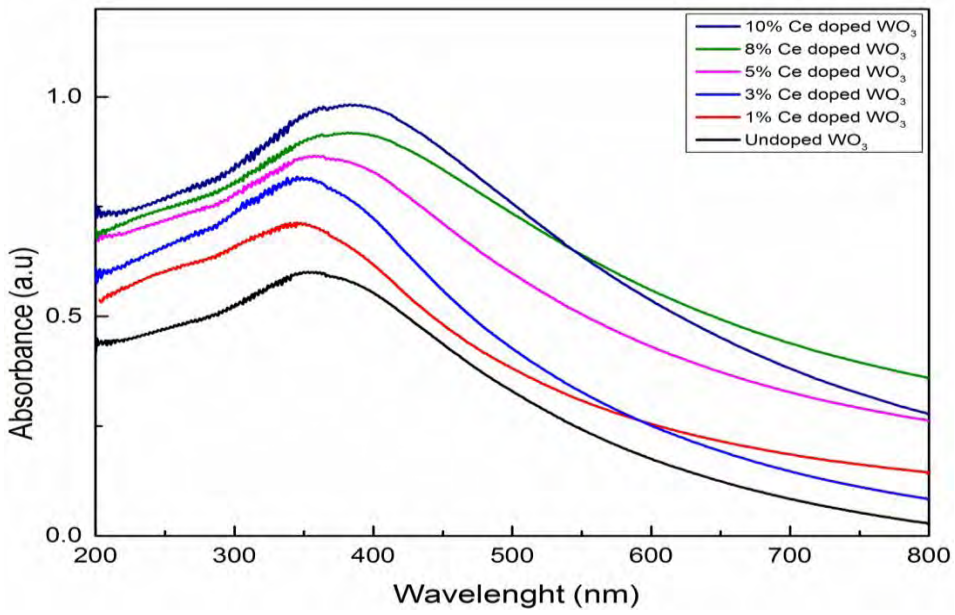

Figure 4.10: UV-visible spectra for prepared samples.

It can be observed from the spectra that the maximum absorption happens in range 338 – 381 nm. It is interestingly fund that undoped sample has absorption at 350 nm but after doping up to 3% Cerium, it shifts to 338 nm while for higher concentration it moves towards 381 nm. This unsystematic variation in absorption with doping is well consistent

with XRD and Raman spectroscopy results. For determining band gap energy "E_g" the plot of "$(\alpha h\nu)^2$" vs "$h\nu$" as shown in the fig 4.11. where "$h\nu$" is photon energy and "α" in absorption coefficient. In case "$h\nu$" (Incident photon energy) is greater than E_g, there is a linear increase in absorption with increase in photon energy but as "$h\nu$" falls down the band gap energy E_g the curve change to nonlinear type.

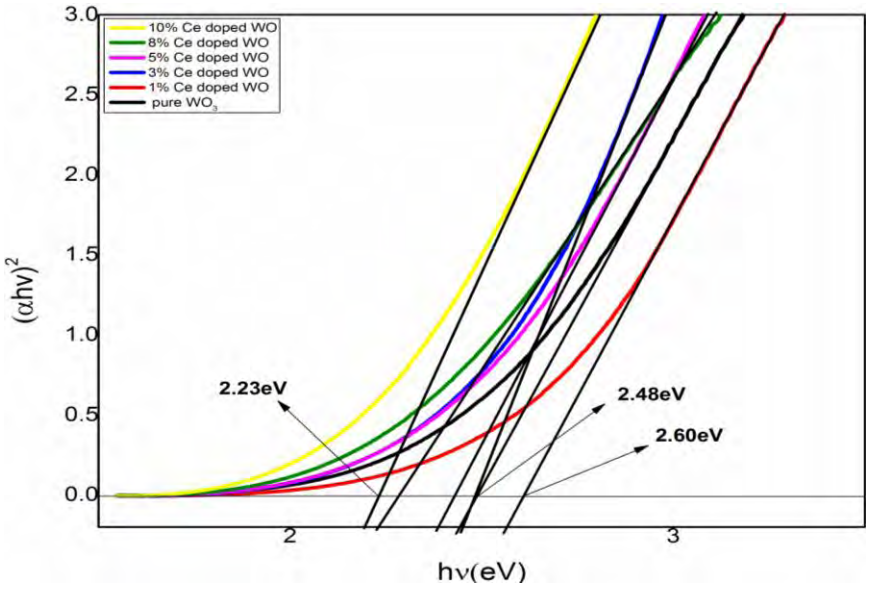

Figure 4.11: Tauc plot for band gap energy (E_g).

Tangent line extrapolated from the linear portion of the graph. The point where tangent line intersects the x-axis gives optical band gap energy. The band gap energy (E_g) for undoped and Ce doped WO_3 nanoparticles are listed in Table 4.3.

Table 4.3: Band gap values for $Ce_xW_{1-x}O_3$ nanoparticles.

Sample name	Working condition	Band gap (eV)
WO_3	Room temperature	2.48
$Ce_{0.01}W_{0.99}O_3$	Room temperature	2.60
$Ce_{0.03}W_{0.97}O_3$	Room temperature	2.40
$Ce_{0.05}W_{0.95}O_3$	Room temperature	2.43
$Ce_{0.08}W_{0.92}O_3$	Room temperature	2.29

$Ce_{0.1}W_{0.9}O_3$	Room temperature	2.23

At high concentration of Ce (>1%) in WO_3 significant decrease in band gap may due to formation of localized states in band gap with Ce doping in WO_3 [61].

4.5 Sun light driven photodegradation of Methylene Blue (MB) dye

Sun light driven photocatalytic activity has been performed for undoped and Ce doped WO_3 nanoparticles to observe their degradation ability against Methylene Blue (MB). The degradation spectra for undoped, 3% and 10% Ce doped WO_3 nanoparticles are shown in figs 4.12, 4.13 and 4.14.

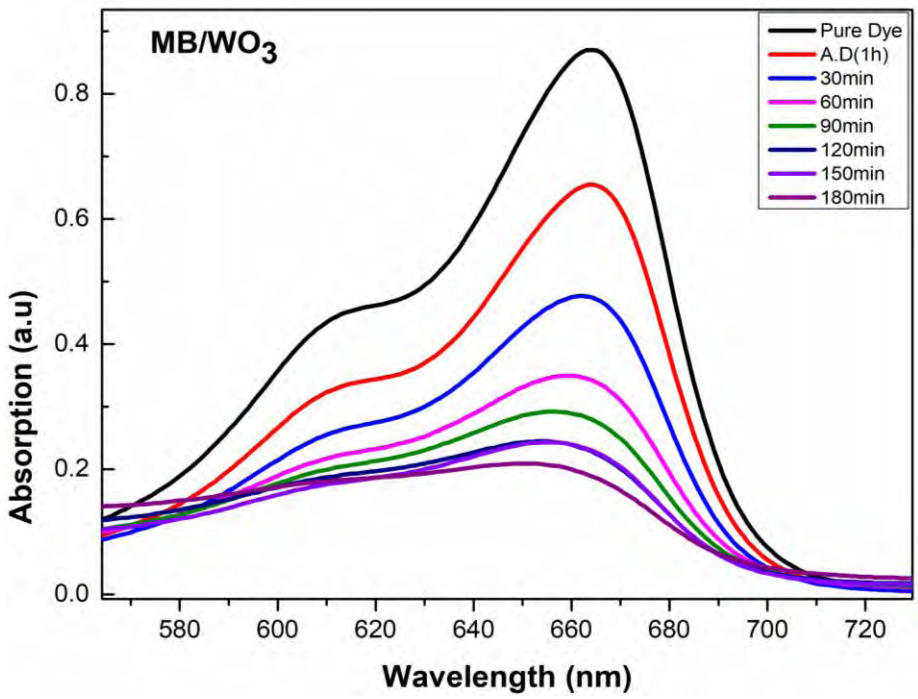

Figure 4.12: Degradation spectra of MB using undoped WO_3 catalyst under sunlight irradiation.

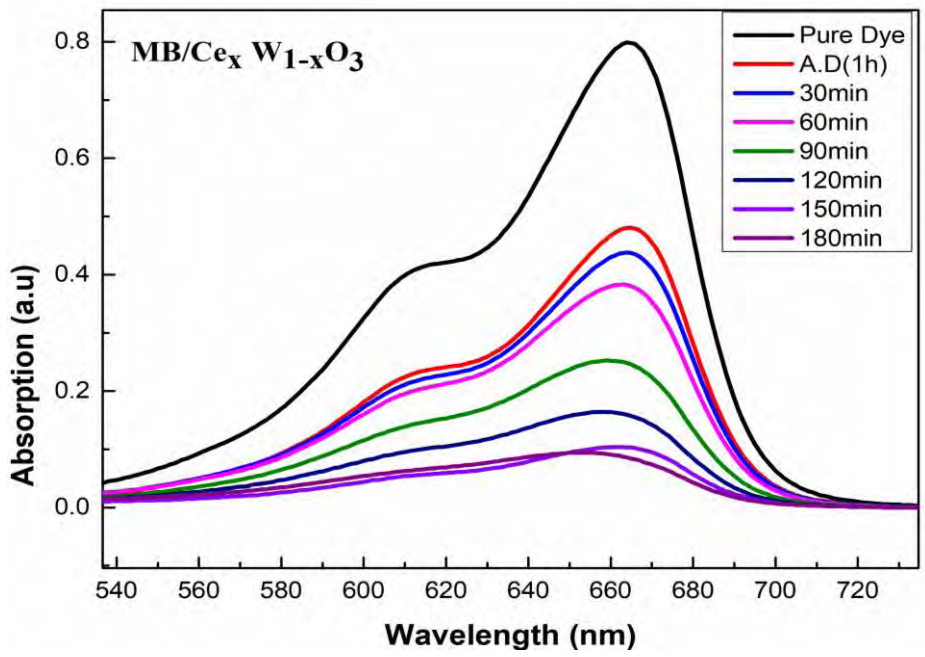

Figure 4.13: Degradation spectra of MB using 3% Ce doped WO_3 catalyst under sunlight irradiation.

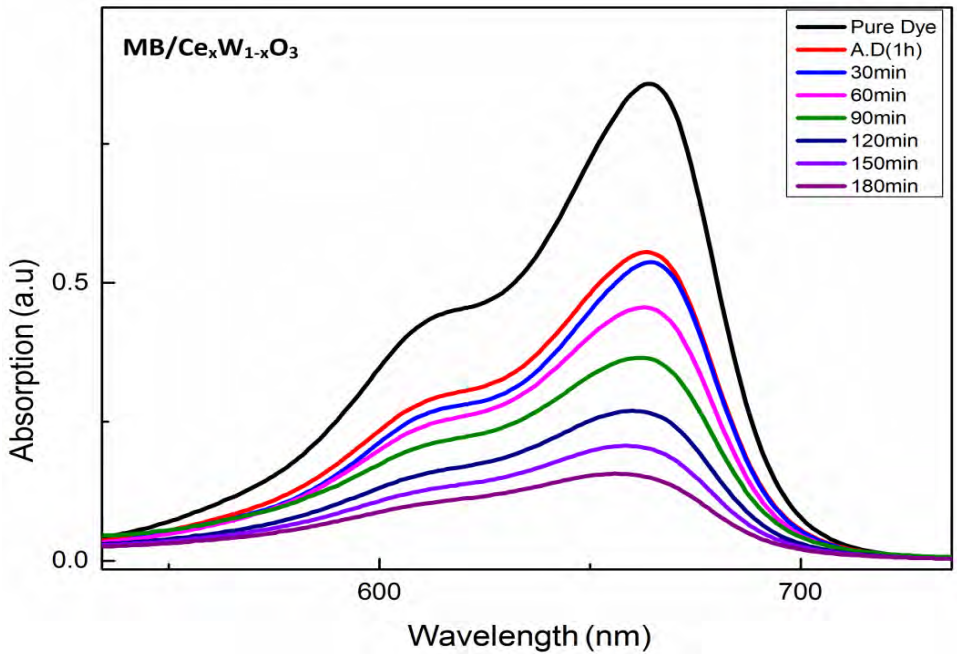

Figure 4.14: Degradation spectra of MB using 10% Ce doped WO_3 catalyst under sunlight irradiation.

The degradation profile of MB in presence of undoped and all Ce doped WO_3 nanoparticles are shown in fig 4.15. The degradation percentage is plotted against length of time. The data in fig 4.15 reveals that the degradation percentage of MB first increases from undoped to 3% Ce doped WO_3 nanoparticles and then decreases with further Ce doping in WO_3. Similar effect of Ce doping on photocatalytic activity of WO_3 was reported by Chang at al [62].

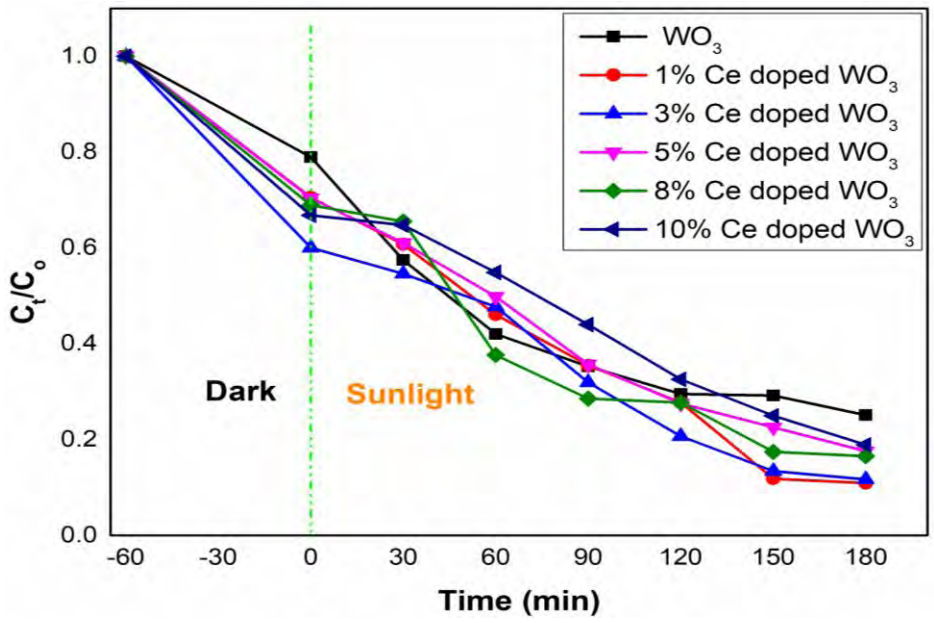

Figure 4.15: Photodegradation of MB by undoped and Ce doped WO_3 nanoparticles.

The bar chart comparison of MB with $Ce_xW_{1-x}O_3$ catalysts for three hours under sunlight is shown in figure 4.16. It is interestingly found that undoped WO_3 nanoparticles have 75% degraded the MB in 3h. Furthermore the Ce doping up to 3% has degraded MB up to 88% in same length of time. However, further $Ce_xW_{1-x}O_3$ (>3%) nanoparticles degradation of MB is up to 80–82%, which is still higher than undoped WO_3 degradation process of MB.

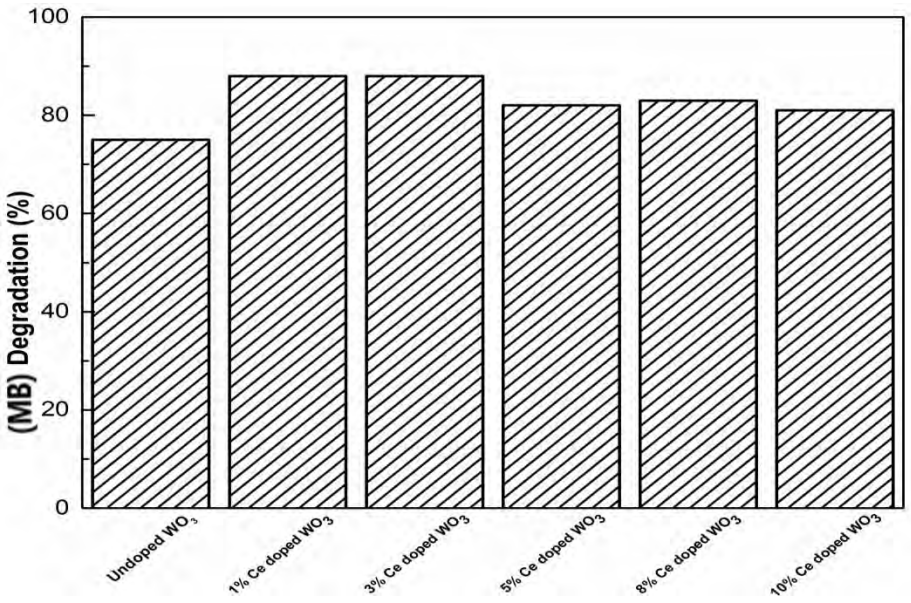

Figure 4.16: Photodegradation percentage of MB using $Ce_xW_{1-x}O_3$ nanoparticles.

In order to check the rate constant of MB degradation, the value of "k" for all Ce (0, 1, 3, 5, 8 and 10%) doped WO_3 are determined by linear fitting as given in fig 4.17.

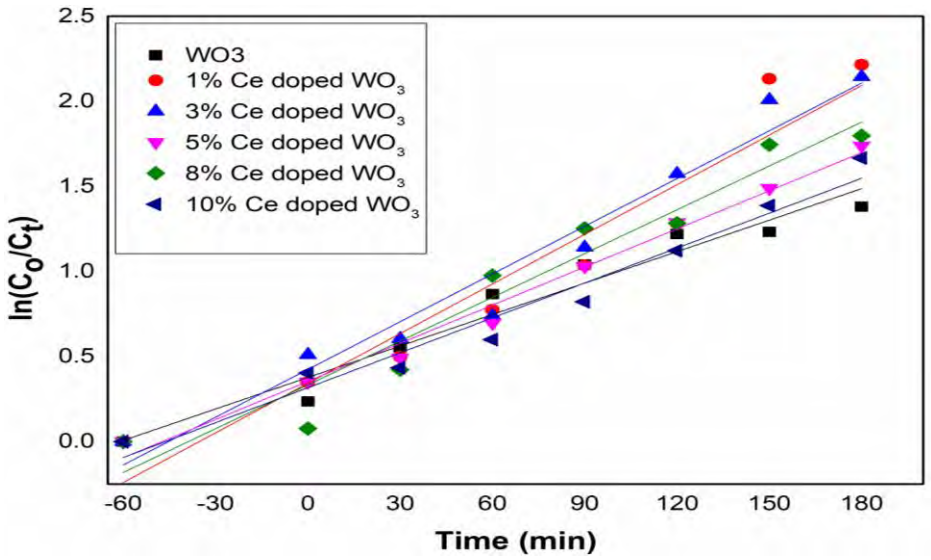

Figure 4.17: Photocatalytic degradation kinetics of MB using Ce (0, 3, 5, 8 and 10%) doped WO_3 catalyst.

To know the general trend in photodegradation activity we focused on undoped, 3% and 10% Ce doped sample linear fitted lines in fig 4.18. The "k" value for undoped

WO_3 sample is 0.00617 min^{-1}, it for 3% Ce doped WO_3 increase up to 0.00935 min^{-1} and then decrease to 0.00684 min^{-1} for 10% Ce doped WO^3 sample.

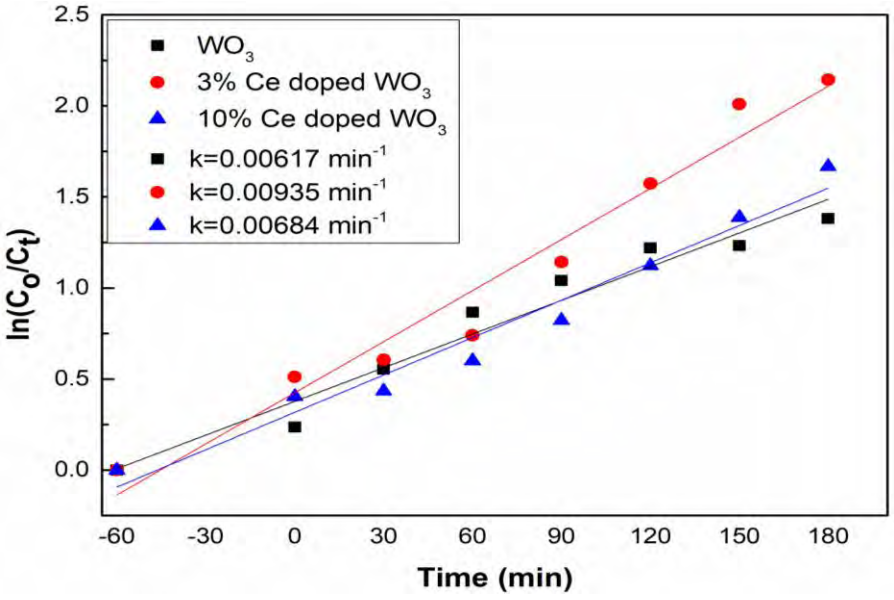

Figure 4.18 Photocatalytic degradation kinetics of MB by undoped WO_3, 3% and 10% Ce doped WO_3 catalyst.

In order to understand the photocatalytic mechanism for MB dye degradation using $Ce_xW_{1-x}O_3$ nanoparticles, a model depicted in fig 4.19. During solar irradiation, catalyst absorbs photons which lead photo-excitation of electrons from valence band to conduction band accompanied with the product of electron-hole pairs. The positive holes in valence band interact with OH^- or H_2O species that adsorbed on the catalyst surface and yield reactive hydroxyl radicals. On the other side, free electron in conduction band react with O_2 to produce super-oxide anions in aqueous media. Super-oxide radical anions act as an additional source of hydroxyl radicals [63].

$$WO_3 + h\upsilon \longrightarrow WO_3(e^- + h^+)$$

$$h^+ + OH^- \longrightarrow {}^{\bullet}OH$$

$$h^+ + H_2O \longrightarrow {}^\bullet OH + H^+$$

$$e^- + H_2O \longrightarrow {}^\bullet O_2^-$$

$${}^\bullet O_2^- + H^+ \longrightarrow {}^\bullet HO_2$$

$$2{}^\bullet HO_2 \longrightarrow H_2O_2 + O_2$$

$$H_2O_2 + {}^\bullet O_2^- \longrightarrow {}^\bullet OH + O_2 + OH^-$$

$$H_2O_2 + h\upsilon \longrightarrow 2{}^\bullet OH$$

The enhancement in degradation activity of Ce doped WO_3, may for two possible seasons. First the decrease in band gap energy (E_g) of WO_3, due to which visible light can generate more electron-hole pairs to take part in degradation processes. While the second reason is that Cerium exists in Ce^{+3}, it also observed in Ce^{+4} too. Ce^{+3} can give an electron to adsorbed O_2 on the surface of Ce doped WO_3 to from ${}^\bullet O_2^-$ and Ce^{+4} [64], it supporting the migration of charge to O_2 and induce enhancement in photoreaction rate comparison with undoped WO_3. Furthermore Ce^{+4}, can receive photogenerated electrons in conduction band of WO_3 to form Ce^{+3}, this reaction could responsibly slow down the recombination rate of photogenerated electron-hole pair and improving interfacial charge transfer efficiency and thus enhancing photocatalytic activity of WO_3 nanoparticles. Further increase in concentration of Ce (>3%) into WO_3 nanoparticles decrease its degradation ability which have two reasons a) increasing concentration of Ce from 3% in WO_3 nanoparticles enlarge crystallite size of nanoparticles. b) Excess Ce (>3%) in WO_3 nanoparticles blocking partial active sits on the surface of WO_3 nanoparticles [63].

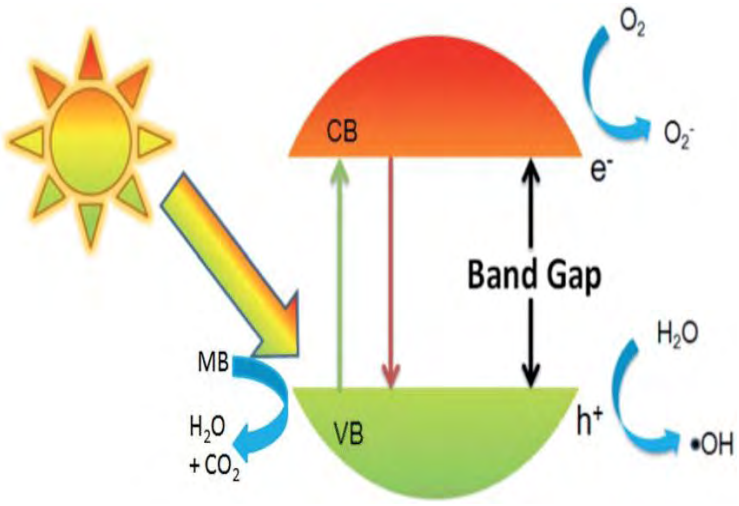

Figure 4.19 Photocatalytic mechanism for WO_3 nanoparticles [65]

Conclusions

The facile co-precipitation method has been employed to synthesis Ce (0, 1, 3, 5, 8 and 10%) doped WO_3 nanoparticles. The structure investigations have confirmed the monoclinic single phase of all samples. Morphological findings reveal the sphere like morphology with average size 80 nm. The vibrational studies has shown that the prepared $Ce_xW_{1-x}O_3$ have stretching, bending and Raman vibrational modes belonging to monoclinic structure of WO_3 with plenty of defects. It is interestingly found that the band gap is significantly tailored with Ce doping which may be due to merging of localized electronic states in band gap region. Furthermore it is found that the photocatalytic activity of prepared samples against MB significantly enhanced with Ce doping into WO_3. These single phase $Ce_xW_{1-x}O_3$ nanoparticles with tailored band gap are potential solar light activated photocatalyst and industrial of waist.

References

1. Harden, D.B., *Ancient Glass, II: Roman.* Archaeological Journal, 1969. **126**(1): p. 44-77.
2. Roco, M.C. and W.S. Bainbridge, *Societal implications of nanoscience and nanotechnology: maximizing human benefit.* Journal of Nanoparticle Research, 2005. **7**(1): p. 1-13.
3. Anand, K., et al., *Structural, optical and gas sensing properties of pure and Mn-doped In 2 O 3 nanoparticles.* Ceramics International, 2016. **42**(9): p. 10957-10966.
4. Kamat, P.V., R. Huehn, and R. Nicolaescu, *A "sense and shoot" approach for photocatalytic degradation of organic contaminants in water.* The Journal of Physical Chemistry B, 2002. **106**(4): p. 788-794.
5. Lee, M.-H., et al., *Nanostructured sorbents for capture of cadmium species in combustion environments.* Environmental science & technology, 2005. **39**(21): p. 8481-8489.
6. Pelizzetti, E. and C. Minero, *Metal oxides as photocatalysts for environmental detoxification.* Comments on Inorganic Chemistry, 1994. **15**(5-6): p. 297-337.
7. Kamat, P.V. and D. Meisel, *Nanoscience opportunities in environmental remediation.* Comptes Rendus Chimie, 2003. **6**(8): p. 999-1007.
8. Averill, B. and P. Eldredge, *General Chemistry: Principles, Patterns, and Applications*2011: The Saylor Foundation.
9. Sun, G., *The intersubband approach to si-based lasers*, in *Advances in Lasers and Electro Optics*2010, InTech.
10. Yoffe, A.D., Adv. Phys, 1993: p. 42-173.
11. Law, M., J. Goldberger, and P. Yang, *Semiconductor nanowires and nanotubes.* Annu. Rev. Mater. Res., 2004. **34**: p. 83-122.
12. Lee, W., et al., *TiO2 nanotubes with a ZnO thin energy barrier for improved current efficiency of CdSe quantum-dot-sensitized solar cells.* Nanotechnology, 2009. **20**(33): p. 335706.
13. Fang, M., et al., *Degradation of nanoRNA is performed by multiple redundant RNases in Bacillus subtilis.* Nucleic acids research, 2009: p. gkp527.
14. Pokropivny, V. and V. Skorokhod, *Classification of nanostructures by dimensionality and concept of surface forms engineering in nanomaterial science.* Materials Science and Engineering: C, 2007. **27**(5): p. 990-993.
15. Kim, Y.T., et al., *Electrochemical Synthesis of CdSe Quantum-Dot Arrays on a Graphene Basal Plane Using Mesoporous Silica Thin-Film Templates.* Advanced Materials, 2010. **22**(4): p. 515-518.
16. Stouwdam, J.W. and R.A. Janssen, *Red, green, and blue quantum dot LEDs with solution processable ZnO nanocrystal electron injection layers.* Journal of Materials Chemistry, 2008. **18**(16): p. 1889-1894.
17. Mokerov, V., et al., *New quantum dot transistor.* Nanotechnology, 2001. **12**(4): p. 552.
18. Bae, S., et al., *Roll-to-roll production of 30-inch graphene films for transparent electrodes.* Nature nanotechnology, 2010. **5**(8): p. 574-578.
19. Tiwari, J.N., R.N. Tiwari, and K.S. Kim, *Zero-dimensional, one-dimensional, two-dimensional and three-dimensional nanostructured materials for advanced electrochemical energy devices.* Progress in Materials Science, 2012. **57**(4): p. 724-803.
20. Kim, K.S., et al., *Large-scale pattern growth of graphene films for stretchable transparent electrodes.* nature, 2009. **457**(7230): p. 706-710.

21. Pradhan, D. and K.T. Leung, *Controlled growth of two-dimensional and one-dimensional ZnO nanostructures on indium tin oxide coated glass by direct electrodeposition.* Langmuir, 2008. **24**(17): p. 9707-9716.
22. Jun, Y.-w., et al., *Recent advances in the shape control of inorganic nano-building blocks.* Coordination chemistry reviews, 2005. **249**(17): p. 1766-1775.
23. Abdelhalim, M.A.K., M.M. Mady, and M.M. Ghannam, *Dielectric constant, electrical conductivity and relaxation time measurements of different gold nanoparticle sizes.* International Journal of Physical Sciences, 2011. **6**(23): p. 5487-5491.
24. Sungpanich, J., T. Thongtem, and S. Thongtem, *Photocatalysis of WO 3 nanoplates synthesized by conventional-hydrothermal and microwave-hydrothermal methods and of commercial WO 3 nanorods.* Journal of Nanomaterials, 2014. **2014**: p. 131.
25. Dong, P., et al., *Highly enhanced photocatalytic activity of WO 3 thin films loaded with Pt–Ag bimetallic alloy nanoparticles.* RSC Advances, 2017. **7**(2): p. 947-956.
26. Madhan, D., et al., *Influence of Zn doping on structural, optical and photocatalytic activity of WO3 nanoparticles by a novel microwave irradiation technique.* Journal of Materials Science. Materials in Electronics, 2015. **26**(9): p. 6823.
27. Das, M.P., *Mesoscopic systems in the quantum realm: fundamental science and applications.* Advances in Natural Sciences: Nanoscience and Nanotechnology, 2010. **1**(4): p. 043001.
28. Guo, D., G. Xie, and J. Luo, *Mechanical properties of nanoparticles: basics and applications.* Journal of Physics D: Applied Physics, 2013. **47**(1): p. 013001.
29. Fahmy, B. and S.A. Cormier, *Copper oxide nanoparticles induce oxidative stress and cytotoxicity in airway epithelial cells.* Toxicology In Vitro, 2009. **23**(7): p. 1365-1371.
30. Sárközi, L., et al., *Subacute intratracheal exposure of rats to manganese nanoparticles: behavioral, electrophysiological, and general toxicological effects.* Inhalation toxicology, 2009. **21**(sup1): p. 83-91.
31. Oszlánczi, G., et al., *Subacute exposure of rats by metal oxide nanoparticles through the airways: general toxicity and neuro-functional effects.* Acta Biologica Szegediensis, 2010. **54**(2): p. 165-170.
32. Pan, X., et al., *Mutagenicity evaluation of metal oxide nanoparticles by the bacterial reverse mutation assay.* Chemosphere, 2010. **79**(1): p. 113-116.
33. Eftekhari, K., et al., *BIOSYNTHESIS AND CHARACTERIZATION OF SILVER AND IRON NANO PARTICLES FROM SPINACIA OLERACEA AND THEIR ANTI CANCER STUDIES IN RAT MODELS.* 2015.
34. Hisatomi, T., J. Kubota, and K. Domen, *Recent advances in semiconductors for photocatalytic and photoelectrochemical water splitting.* Chemical Society Reviews, 2014. **43**(22): p. 7520-7535.
35. Hoffmann, M.R., et al., *Environmental applications of semiconductor photocatalysis.* Chemical reviews, 1995. **95**(1): p. 69-96.
36. Ahmed, A.B., R. Konwar, and R. Sengupta, *Atorvastatin calcium loaded chitosan nanoparticles: in vitro evaluation and in vivo pharmacokinetic studies in rabbits.* Brazilian Journal of Pharmaceutical Sciences, 2015. **51**(2): p. 467-477.
37. Buzea, C., I.I. Pacheco, and K. Robbie, *Nanomaterials and nanoparticles: Sources and toxicity.* Biointerphases, 2007. **2**(4): p. MR17-MR71.
38. Chandradass, J., D.S. Bae, and K.H. Kim, *A simple method to prepare indium oxide nanoparticles: structural, microstructural and magnetic properties.* Advanced Powder Technology, 2011. **22**(3): p. 370-374.
39. Zheng, H., et al., *Nanostructured tungsten oxide–properties, synthesis, and applications.* Advanced Functional Materials, 2011. **21**(12): p. 2175-2196.
40. Castellote, M. and N. Bengtsson, *Principles of TiO2 photocatalysis*, in *Applications of Titanium Dioxide Photocatalysis to Construction Materials*2011, Springer. p. 5-10.

41. Wu, P.M., et al., *Synthesis and ionic liquid gating of hexagonal WO3 thin films.* Applied Physics Letters, 2015. **106**(4): p. 042602.
42. Roussel, P., P. Labbe, and D. Groult, *Symmetry and twins in the monophosphate tungsten bronze series (PO2) 4 (WO3) 2m (2≤ m≤ 14).* Acta Crystallographica Section B: Structural Science, 2000. **56**(3): p. 377-391.
43. Woodward, P., A. Sleight, and T. Vogt, *Ferroelectric tungsten trioxide.* Journal of solid state chemistry, 1997. **131**(1): p. 9-17.
44. P. M. Woodward, A.W.S., T. Vogt, Solid State Chem, 1997
45. K. K. Zhu, H.Y.H., S. H. Xie , X. Zhang , W. Z. Zhou , S. L. Jin ,B. Yue, Chem. Phys. Lett., 2003: p. 377 , 317.
46. Salje, E.K., et al., *Crystal structure and paramagnetic behaviour of.* Journal of Physics: Condensed Matter, 1997. **9**(31): p. 6563.
47. Vogt, T., P.M. Woodward, and B.A. Hunter, *The high-temperature phases of WO3.* Journal of Solid State Chemistry, 1999. **144**(1): p. 209-215.
48. Gerand, B., et al., *Structural study of a new hexagonal form of tungsten trioxide.* Journal of Solid State Chemistry, 1979. **29**(3): p. 429-434.
49. Desre, P., *A thermodynamic model for the nanocrystal to glass transition of intermetallic compounds subjected to high deformation by mechanical attrition—Application to L1 2 phases.* Nanostructured materials, 1997. **8**(6): p. 687-701.
50. Bignozzi, C.A., et al., *Nanostructured photoelectrodes based on WO 3: applications to photooxidation of aqueous electrolytes.* Chemical Society Reviews, 2013. **42**(6): p. 2228-2246.
51. Gullapalli, S., R. Vemuri, and C. Ramana, *Structural transformation induced changes in the optical properties of nanocrystalline tungsten oxide thin films.* Applied Physics Letters, 2010. **96**(17): p. 171903.
52. Yoffe, A.D., *Low-dimensional systems: quantum size effects and electronic properties of semiconductor microcrystallites (zero-dimensional systems) and some quasi-two-dimensional systems.* Advances in Physics, 1993. **42**(2): p. 173-262.
53. Yin, J., et al., *Synthesis and applications of γ-tungsten oxide hierarchical nanostructures.* Crystal Growth & Design, 2013. **13**(2): p. 759-769.
54. Lee, S.H., et al., *Crystalline WO3 nanoparticles for highly improved electrochromic applications.* Advanced Materials, 2006. **18**(6): p. 763-766.
55. Marques, A., et al., *Office Paper Platform for Bioelectrochromic Detection of Electrochemically Active Bacteria using Tungsten Trioxide Nanoprobes.* Scientific reports, 2015. **5**.
56. Zhang, H., et al., *Tungsten oxide nanostructures based on laser ablation in water and a hydrothermal route.* CrystEngComm, 2014. **16**(12): p. 2491-2498.
57. Mehmood, F., et al., *Effect of Sn doping on the structural, optical, electrical and anticancer properties of WO 3 nanoplates.* Ceramics International, 2016. **42**(13): p. 14334-14341.
58. Chen, D., et al., *Effects of boron doping on photocatalytic activity and microstructure of titanium dioxide nanoparticles.* Industrial & Engineering Chemistry Research, 2006. **45**(12): p. 4110-4116.
59. Delichere, P., et al., *Electrochromism in anodic WO3 films I: preparation and physicochemical properties of films in the virgin and coloured states.* Thin Solid Films, 1988. **161**: p. 35-46.
60. Arshad, A., et al., *Graphene nanoplatelets induced tailoring in photocatalytic activity and antibacterial characteristics of MgO/graphene nanoplatelets nanocomposites.* Journal of Applied Physics, 2017. **121**(2): p. 024901.
61. Mehmood, F., et al., *Facile synthesis of 2-D Cu doped WO 3 nanoplates with structural, optical and differential anti cancer characteristics.* Physica E: Low-dimensional Systems and Nanostructures, 2017. **88**: p. 188-193.

62. Chang, X., et al., *Solvothermal synthesis of Ce-doped tungsten oxide nanostructures as visible-light-driven photocatalysts.* Nanotechnology, 2011. **22**(26): p. 265603.
63. Liu, H., et al., *Preparation and photocatalytic activity of dysprosium doped tungsten trioxide nanoparticles.* Materials Chemistry and Physics, 2007. **104**(2): p. 377-383.
64. Sclafani, A., et al., *Influence of platinum on catalytic activity of polycrystalline WO3 employed for phenol photodegradation in aqueous suspension.* Solar energy materials and solar cells, 1998. **51**(2): p. 203-219.
65. Husanu, E., et al., *Chiral ionic liquid assisted synthesis of some metal oxides.* RSC Advances, 2017. **7**(2): p. 1154-1160.

Plagiarism Report